

FeNb11O29, anode material for high-power lithium-ion batteries: Pseudocapacitance and symmetrisation unravelled with advanced electrochemical and in situ/operando techniques

Original

FeNb11O29, anode material for high-power lithium-ion batteries: Pseudocapacitance and symmetrisation unravelled with advanced electrochemical and in situ/operando techniques / Spada, D.; Albin, B.; Galinetto, P.; Versaci, D.; Francia, C.; Bodoardo, S.; Bais, G.; Bini, M.. - In: ELECTROCHIMICA ACTA. - ISSN 0013-4686. - ELETTRONICO. - 393:(2021), p. 139077. [10.1016/j.electacta.2021.139077]

Availability:

This version is available at: 11583/2929114 since: 2021-10-05T11:54:56Z

Publisher:

Elsevier Ltd

Published

DOI:10.1016/j.electacta.2021.139077

Terms of use:

This article is made available under terms and conditions as specified in the corresponding bibliographic description in the repository

Publisher copyright

(Article begins on next page)

**FeNb₁₁O₂₉, anode material for high-power lithium-ion batteries:
Pseudocapacitance and symmetrisation unravelled with advanced
electrochemical and in situ/operando techniques**

Daniele Spada ^a, Benedetta Albini ^b, Pietro Galinetto ^b, Daniele Versaci ^c, Carlotta Francia ^c, Silvia Bodoardo ^c, Giorgio Bais ^d, Marcella Bini ^{a*}

^a Dept. of Chemistry, University of Pavia, viale Taramelli 16, 27100 Pavia, Italy

^b Dept. of Physics, University of Pavia, via Bassi 6, 27100 Pavia, Italy

^c Department of Applied Science and Technology (DISAT), Politecnico di Torino, C.so Duca degli Abruzzi 24, 10129 Torino, Italy

^d Elettra Sincrotrone Trieste, Area Science Park, 34149 Basovizza, Italy

*** Corresponding Author**

Marcella Bini, Dept. of Chemistry, University of Pavia, viale Taramelli 16, 27100 Pavia, Italy;

e-mail: bini@unipv.it

Abstract

In the last years of research on new anode materials for advanced Lithium-Ion Batteries (LIBs), niobium-based oxides are raising more and more attention due to very high theoretical capacities and high working potential that can prevent the formation of SEI film and lithium dendrites, ensuring the safety of the batteries. Most of the M–Nb–O family crystallize in Wadsley–Roth shear structures, which are built of $m \times n \times \infty$ ReO_3 -type blocks of octahedra. Such open structures can lead to large Li-ion diffusion coefficients, which shows promising applications in energy storage systems.

In this paper, an overview of the state-of-the-art structural and electrochemical features of $\text{FeNb}_{11}\text{O}_{29}$ (which is known as anode material for LIBs since 2014) is given. Results of previous works are accompanied by novel findings, **that unravel** the complex behaviour of the system.

The lithiation reaction and the related electrochemistry were characterized with *in situ* Raman Spectroscopy, *operando* X-Ray Diffraction and the most widespread electrochemical techniques. The intrinsic pseudocapacitance shown by the niobate was analysed and correlated to the structural evolution of the pristine phase. The symmetrisation of the octahedral framework that occurs after the reduction of Nb^{5+} cations was determined to be vital for the electrochemistry of $\text{FeNb}_{11}\text{O}_{29}$, that shows excellent features for advanced high-power density LIBs.

Keywords: $\text{FeNb}_{11}\text{O}_{29}$; Niobium oxides; Shear structures; Lithium-ion batteries; in-situ, *operando*, Pseudocapacitance

1. Introduction

The extensive use of fossil fuels, such as oil, gas, and coal, has vastly promoted the development of world economy. However, the rapid consumption of these non-renewable resources brought enormous interest in effective alternatives to fossil energy, resulting in the research boom for various clean energy sources such as solar, wind, tide, and geothermal energies.¹ Unfortunately, the inherent regional and intermittent disadvantages of these clean energies limited their applications in many fields. An efficient strategy to address this issue is to exploit energy storage and conversion technologies to gather the scattered energy. Until now, the most widely used energy storage systems for various electronic devices and electric vehicles have been the rechargeable batteries and electrochemical capacitors.¹

Lithium-ion batteries (LIBs) as one typical representative of secondary batteries have revolutionized our lives: laptops, mobile phones and numerous microelectronic devices could not survive without LIBs. As we know, the rechargeable batteries are mainly composed of electrode materials, separators, and electrolytes. Among them, electrode materials play a vital role in improving the electrochemical performances. Cathode materials generally are lithium-containing compounds, (e.g. LiCoO_2 , LiMn_2O_4 , $\text{Li}_2\text{MnSiO}_4$ and so on)² but this makes the selection of cathode materials limited. **On the contrary, any material that can reversibly store Li-ions with a suitable potential window can serve as anode material.** Numerous anode materials including carbon-based,³ TiO_2 ,⁴ $\text{Li}_4\text{Ti}_5\text{O}_{12}$,⁵ Nb_2O_5 ⁶ are the popular intercalation-type electrodes. Developing advanced intercalation-type anode materials can significantly enhance the electrochemical performances of battery systems. In addition, owing to the increasing demand for electric vehicles and hybrid electric vehicles, the hybrid supercapacitors (HSCs) have captured tremendous research interests.⁷ HSCs are made up of capacitor-type cathode and battery-type anode. However, the slow redox reactions derived from battery-type anodes hinder the electrochemical performances of the overall HSCs.⁸ Therefore, developing superior intercalation-type anode materials with fast charge-discharge storage capability has a vital role.¹

While strategies like nanostructuring have been used extensively to improve high-rate performance in materials like $\text{Li}_4\text{Ti}_5\text{O}_{12}$,⁹ this has many drawbacks including high cost, poor stability, and poor volumetric energy density. However, nanostructuring is not the primary request to obtain high rates. Recent works have shown that very high rates can be achieved in micrometre-sized particles of complex oxides of niobium.^{10,11}

Niobium-based oxides anodes are raising more and more attention thanks to very high theoretical capacities ($\text{Nb}_2\text{O}_5 \approx 200 \text{ mAh g}^{-1}$ and $\text{TiNb}_x\text{O}_{2+2.5x}$ compounds $\approx 388\text{--}401 \text{ mAh g}^{-1}$).^{12,13} Niobium-based oxides are a big family including Nb_2O_5 , TiNb_2O_7 , $\text{Ti}_2\text{Nb}_{10}\text{O}_{29}$, $\text{TiNb}_6\text{O}_{17}$,

TiNb₂₄O₆₂ and so on. Most of Ti–Nb–O family can be described using the chemical formula as TiNb_xO_{2+2.5x}, with a Wadsley–Roth shear crystal structure, built by $m \times n \times \infty$ ReO₃-type blocks (m and n represent the length and width of the blocks, in numbers of octahedra). Such open Wadsley–Roth shear structures can lead to large Li-ion diffusion coefficients, which is beneficial for energy storage systems. In addition, TiNb_xO_{2+2.5x} family have a high operating voltage of ≈ 1.6 – 1.7 V (vs Li⁺/Li), which can match well with the lowest unoccupied molecular orbital (LUMO) of the organic liquid-carbonate electrolyte, avoiding the formation of solid–electrolyte interphase (SEI) layer and lithium dendrite and ensuring the safety of batteries. ¹

However, the intrinsic low electrical conductivity and Li-ion diffusion coefficients hinder their practical applications in LIBs. In view of these two factors, exploring anode materials with similar structural merits to TiNb_xO_{2+2.5x} compounds but with intrinsic higher electrical conductivity and larger Li-ion diffusion coefficients is significant and challenging. The Li-ion diffusion coefficients are very sensitive to the unit cell volume, therefore, using appropriate transition metal ions to replace M sites in M–Nb–O family can be expected to perform improved electrochemical performances. ¹

The use of FeNb₁₁O₂₉ in electrochemical cells was suggested in 2014. ¹⁴ Taking advantage of the Niobium reductions (from 5+ to 4+ and 3+), it can store 23 Li⁺ ions per formula unit, giving a theoretical capacity of 400 mAh/g, one of the highest among intercalation anodes. It shares the features of M–Nb–O oxides, such as safety, good rate capability and cycling stability, but also the main drawback of the poor electronic conductivity (only the electrons deriving from Fe³⁺ can participate to the electronic conduction). To tackle this issue, some authors attempted, successfully, the doping ^{15,16} or the introduction of oxygen vacancies. ¹⁷ Another way of improving the performances is the nanostructuration, which is not required as for most electrode materials, but still beneficial in terms of the reduction in the diffusion or transport distance of the Li ions and electrons. In 2019, FeNb₁₁O₂₉ nanotubes were employed both in test and in full cells with LiCoO₂, LiMn₂O₄ and LiFePO₄, showing promising results. ¹⁸

In this paper, an overview of the structural features of FeNb₁₁O₂₉ is given, together with a detailed discussion on the lithiation reaction and the related electrochemistry.

With the help of *in situ* Raman Spectroscopy and *operando* X-Ray Diffraction, the intercalation of Li⁺ ions in both polymorphs of FeNb₁₁O₂₉ (monoclinic and orthorhombic) was characterized, allowing the experimental observation of the symmetrisation of the octahedral framework that occurs after the reduction of Nb⁵⁺ cations, which was determined to be vital for the electrochemistry of FeNb₁₁O₂₉.

The intrinsic pseudocapacitance shown by the niobate was correlated to the structural evolution of the pristine phase, thanks to common and advanced electrochemical techniques such as Cyclic Voltammetry (CV), Galvanostatic Cycling with Potential Limitations (GCPL), Electrochemical Impedance Spectroscopy (EIS) and Galvanostatic Intermittent Titration Technique (GITT). Each of those techniques allowed the observation of different and complementary aspects of the features of the iron niobate, showing its potential as anode material for advanced LIBs.

2. Results and discussion

In this section, an overview of previous works¹⁴⁻²³ will be given in order to make clearer the discussion of *in situ/operando* techniques.

2.1 The structure of pristine FeNb₁₁O₂₉

FeNb₁₁O₂₉ belongs to the family of shear structures deriving from Nb₂O₅, called Wadsley-Roth phases, which consist of blocks of m x n octahedra which are piled up in a way that infinite columns of blocks are formed. The columnar structure is responsible for the interesting magnetic features observed in Nb₁₂O₂₉ (an antiferromagnet oxide with metallic conductivity)²⁴, but also for the electrochemical behaviour of this class of compounds: the perovskitic cavities of the ReO₃-like blocks are linked each other in a 3-D way, offering wide and interconnected tunnels for fast Li⁺ intercalation.

For the early transition metal oxides which have 3-D blocks of corner-shared MO₆ octahedra as their basic structural component, changing the oxygen stoichiometry causes large-scale structural rearrangement. The blocks are broken along planes of shared corners and shifted, to eliminate whole planes of oxygen atoms, creating planes of edge-shared octahedra. This “crystallographic shear” process results in long-range ordered arrays of 2-D planes of edge-shared octahedra dressing the edges of the 3-D corner-shared blocks. The fully oxidized insulating Nb⁵⁺ oxide, Nb₂O₅, occurs in many polymorphic forms with crystallographic shear structures. On chemical reduction of Nb by oxygen removal, a whole series of related crystallographic shear structures is formed. Nb₁₂O₂₉ is the most stable of the reduced phases occurring between Nb₂O₅ (Nb⁵⁺) and NbO₂ (Nb⁴⁺).²⁴

Many phases with general formula M_xNb_{12-x}O₂₉ are already reported in literature, and their characteristic feature is dimorphism (monoclinic or orthorhombic symmetry). Both the phases belong to the double shear type: in their structures n x m x ∞ ReO₃-type blocks (previously called 3-D corner shared blocks) occur. Neighbouring blocks share common edges, half of the at the level y = 0 and the other half at y = 0.5. The monoclinic and the orthorhombic phases differ by the manner of linking individual blocks (Fig. 1). The monoclinic polymorph is obtained at temperatures from

900 to 1100 °C, depending on the synthesis. The orthorhombic polymorph can be obtained from the monoclinic one, after an irreversible phase transition occurring at 1250°C.¹⁹

In the orthorhombic form, the cell has an orthogonal symmetry because blocks share *cis* corners with blocks at the same level, while in the monoclinic form, the blocks share *trans* corners. The rearrangement of the columns on going from the monoclinic to the orthorhombic form has both long range and local effects: on the nanometre scale, the structures differ only for about a 3 nm translation in one of their three dimensions, while on the angstrom scale, the symmetry of the crystal structures change because a mirror plane is missing in the monoclinic form, and all the local symmetries are thus correspondingly lowered.²¹

The structures are overall quite similar, as the XRD patterns in Fig. 1 indicate. However, little differences caused by the linking between blocks can be detected (Figure S1).

This kind of structures is often described as a ReO_3 -like structure because ReO_3 (which is constituted only by corner sharing octahedra) has similar cavities, that are called perovskitic because ReO_3 can be considered as a cubic perovskite ABO_3 without the cation A. Upon lithiation, those cavities undergo an irreversible twisting that originates 2 smaller octahedral sites from a single cavity, because each cavity is too large for a proper coordination of a single Li^+ ion.²⁵ In $\text{FeNb}_{11}\text{O}_{29}$ this twisting is prevented because edge-sharing octahedra make the structure less flexible, giving wide, open tunnels weakly coordinating Li^+ ions.

Another feature of this family of niobium oxides is the disorder involving framework cations, observed with neutron diffraction studies¹⁰ and foreseen from the sloping charge/discharge potential profiles (also observed in amorphous materials), which arise from the nonequivalent site energy due to the disordered cations. The cation disorder has a significant effect on the local structure in niobium oxide shear phases: a lithium ion within a disordered niobium oxide shear structure experiences different local environments from one unit cell to the next. This randomness in the potential energy landscape of the lithium ions in a disordered structure suppresses lithium ordering and makes a larger number of sites available for occupation, resulting in a favourable attribute to enhance electrochemical performances.¹⁰

This concepts can be applied to $\text{FeNb}_{11}\text{O}_{29}$: its sloping profile cannot be explained with amorphization ($\text{Li}_x\text{FeNb}_{11}\text{O}_{29}$ is crystalline)^{14,18}. Instead, Fe^{3+} cations are distributed all over the different crystallographic sites (Fig. S2), affecting the local environment that lithium ions experience from one unit cell to the next.

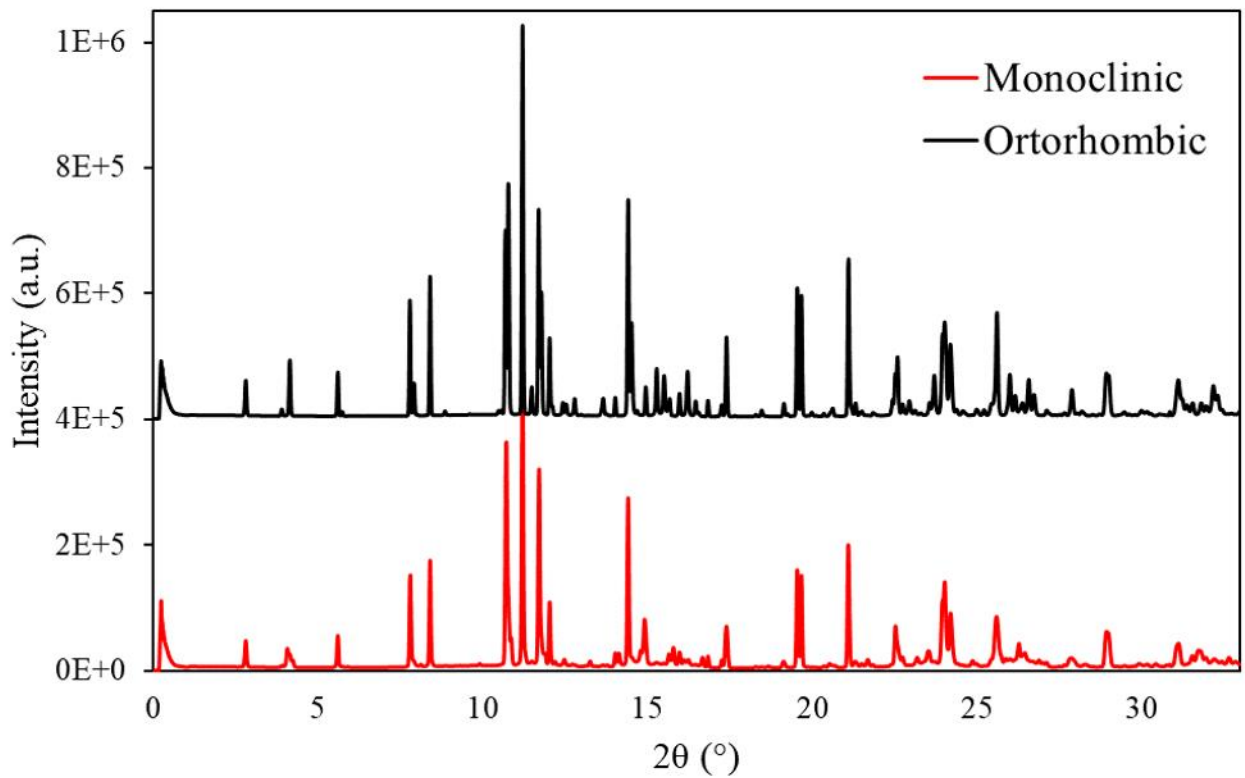
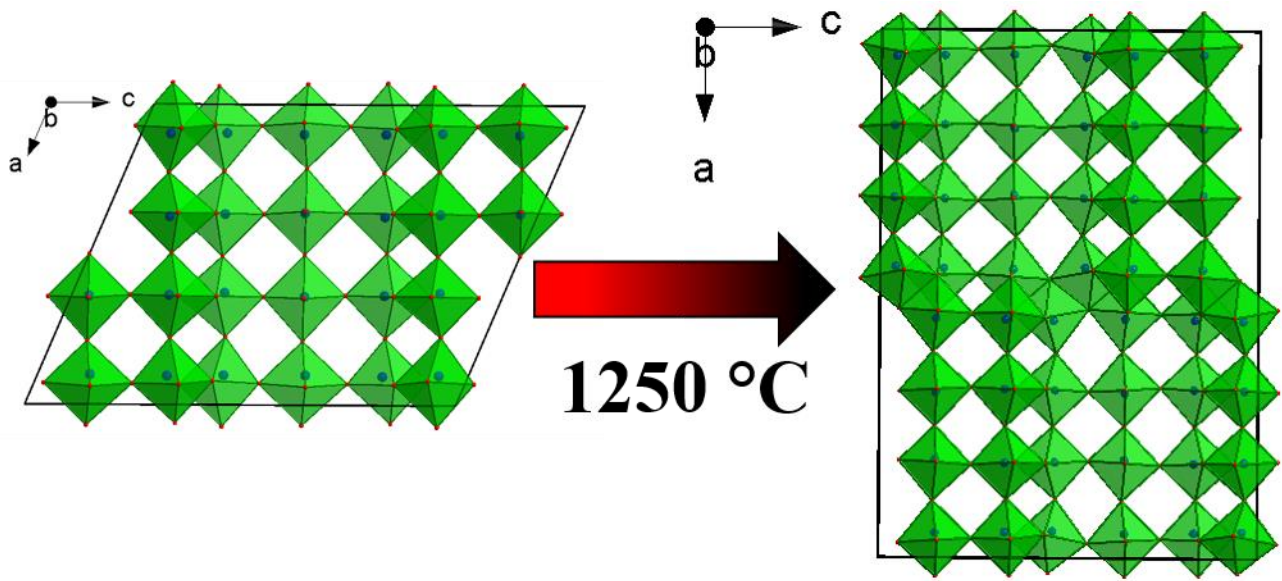


Fig. 1 – Unit cell of both monoclinic and orthorhombic $\text{FeNb}_{11}\text{O}_{29}$, along with synchrotron XRD powder patterns.

2.2 Overall structural evolution

In situ measurements and, in particular, *operando* measurements can reveal valuable information about the electrode materials without disassembling the testing cells and can aid establishing correlations between structural properties and electrochemical performances. Each technique has unique capabilities to study specific properties of the electrode materials (structure evolution, redox mechanism, SEI formation, side reactions, Li-ion transport properties and so on).²⁶

2.2.1 Diffraction

In situ/operando X-Ray Diffraction (XRD) is widely used to study the crystal structures and phase transformations in electrode and solid electrolyte materials for LIBs during cycling.²⁶

Pinus et al¹⁴ performed neutron powder diffraction experiments on a partially lithiated phase ($\text{Li}_{11}\text{FeNb}_{11}\text{O}_{29}$), observing a non-negligible cell expansion upon lithiation, with a volume increase of 6.1%. The expansion was determined to be highly anisotropic: the building blocks of 4 x 3 octahedra are slightly deformed ($a - 1.1\%$, $c + 0.4\%$) and repel each other ($b + 6.8\%$), becoming a quasi-layered structure, hosting Lithium ions in between planes of building blocks. This experimental observation easily explains the neat and parallel fractures observed in our previous work¹⁶, that are then attributed to the expansion of the [0 k 0] planes.

In situ XRD data on monoclinic $\text{FeNb}_{11}\text{O}_{29}$ nanotubes are already reported in literature¹⁸, confirming the lattice volume expansion (6.92%) in the lithiation process, which was also determined to be reversible. The authors divided electrochemical curves of the intercalation reaction in regions, corresponding to 2 solid solution regions and two-phase-like region in between, finding that all the parameters expand, except in the two-phase-like region where a shrinks.

Computational data on the related oxide $\text{Nb}_{12}\text{WO}_{33}$ ¹⁰ predicted the anisotropic expansion, but in a slightly different way: the lattice should evolve through three regions, with the lattice parameter perpendicular to the plane of the block (b in our case) expanding monotonically, while in the block plane the lattice parameters (a and c) expand, contract, and then expand again. The two-phase-like region, marked by a symmetrisation of the MO_6 octahedra, makes previously highly distorted sites available for lithium occupation and allows neighbouring blocks to slide closer together, causing the lattice contraction within the block plane.¹⁰

For the oxides $\text{Nb}_{12}\text{WO}_{33}$ and $\text{Nb}_{16}\text{W}_5\text{O}_{55}$, the results of micron-sized materials agree with DFT prediction, while the results obtained by chemically lithiated material or nanosized material

differ strongly for what concerns the structural evolution of the materials. Hence, the importance of a study involving synchrotron radiation on proper samples.

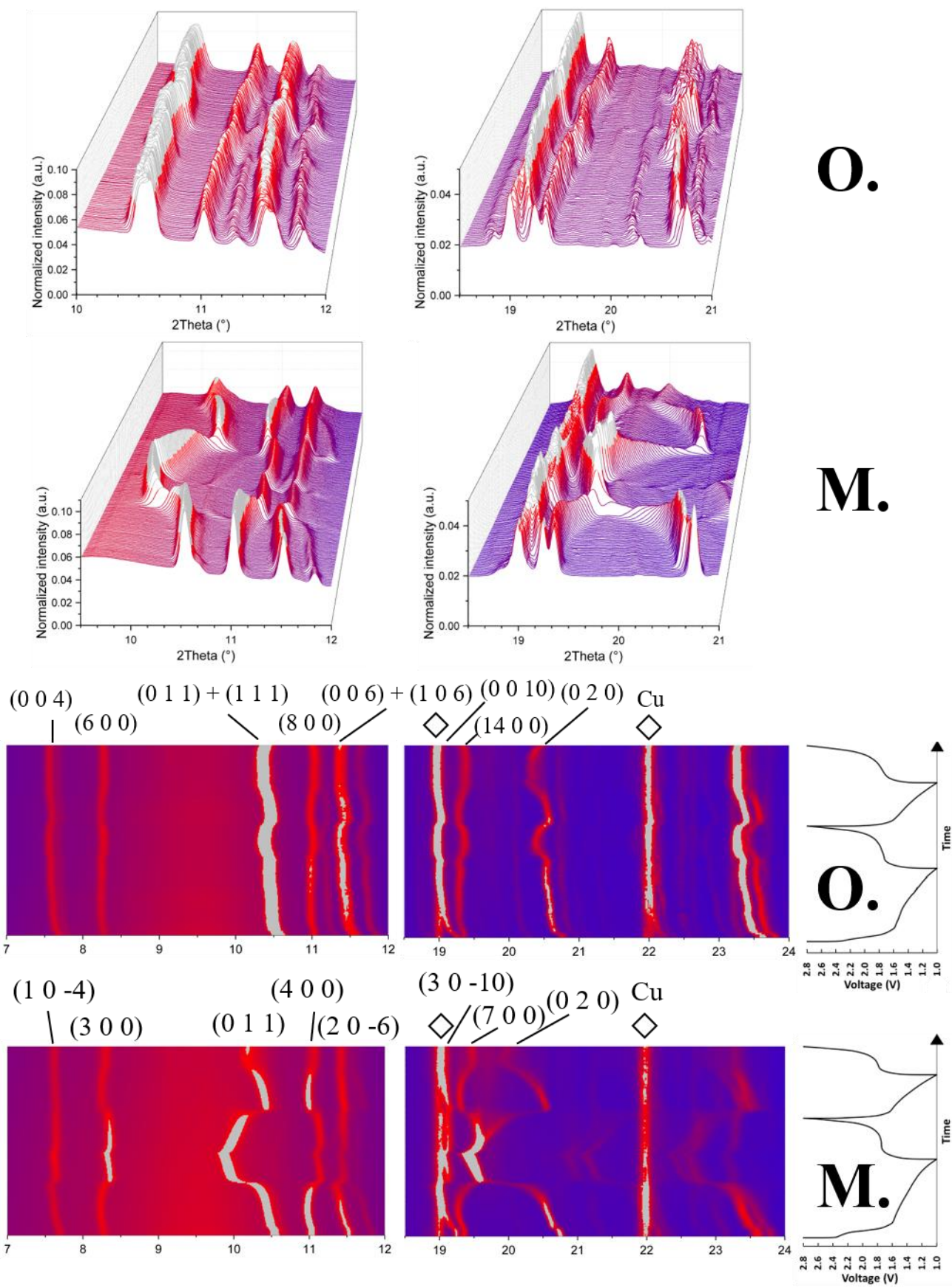


Figure ?? – Operando XRD patterns for both the samples, along with magnified regions.

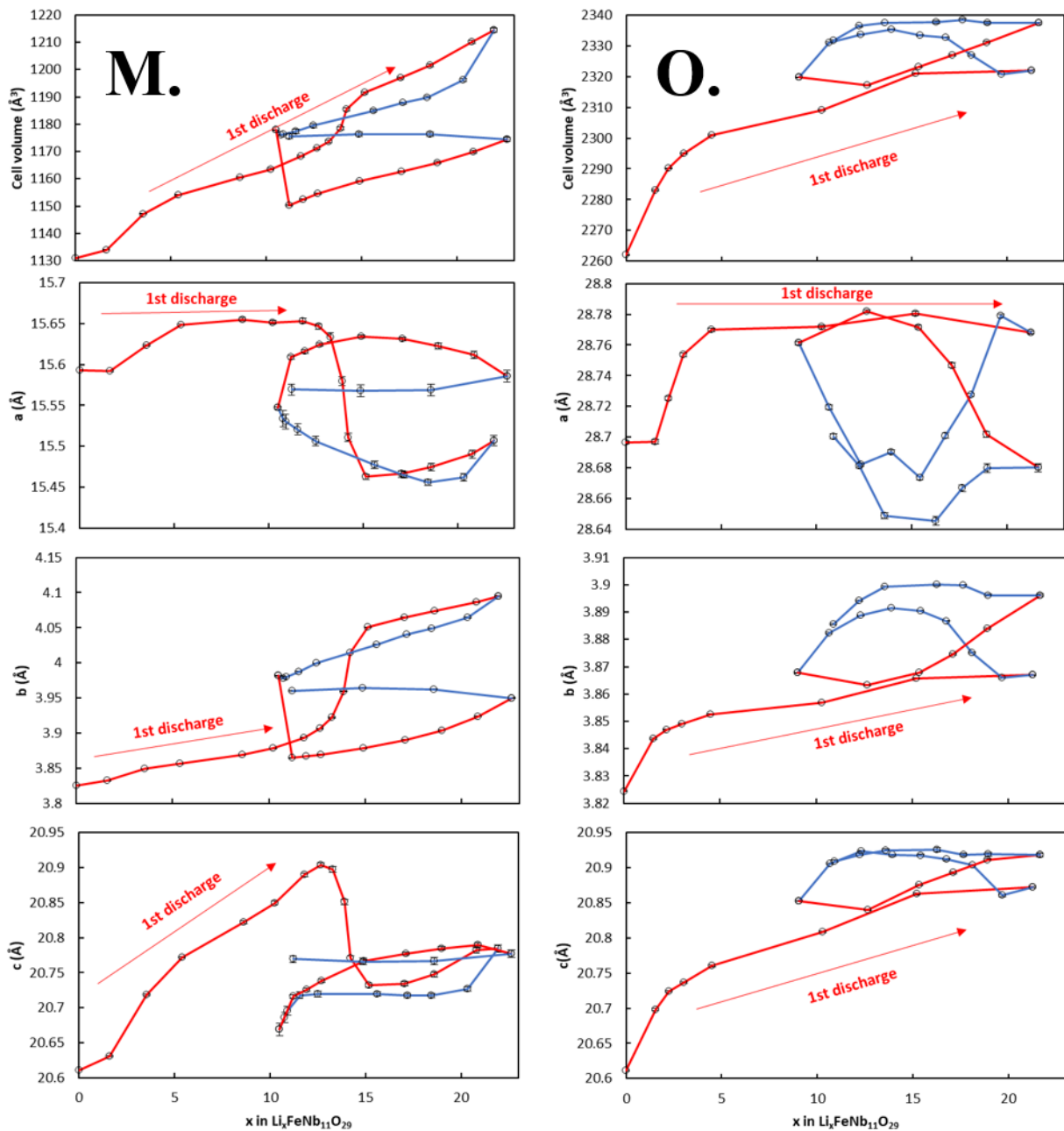


Figure 2 – Refined lattice parameters, for both samples, during *operando* XRD measurements at a low current (C/10). M. and O. stand for monoclinic and orthorhombic.

In fig. 2 the *operando* XRD patterns of $\text{FeNb}_{11}\text{O}_{29}$ are shown, together with ????. The detailed analysis of the multiple components evidenced in the first pattern, collected at the OCV of the cells, is reported in the Supporting Information (Fig. S3). Aside from the current collector, the diffraction peaks can be assigned to $\text{FeNb}_{11}\text{O}_{29}$ for the duration of the whole measurements. Because of the solid-solution behavior manifested during Lithium intercalation, the lattice parameters of $\text{FeNb}_{11}\text{O}_{29}$

were refined vs the amount of Li intercalated in the structure of $\text{FeNb}_{11}\text{O}_{29}$ (which is directly proportional to the measured capacity).

Operando XRD data shown in Fig. 2 well agree with DFT calculations but differ from those on $\text{FeNb}_{11}\text{O}_{29}$ nanotubes with *in situ* diffraction.¹⁸ One of the reasons can be attributed to the particles sizes (micron- vs nano-sized), and the other is the timescale of the experiment, that can drastically affect the final results, as we will see later in the paper. It can also be inferred that the nanostructuration suppresses the predicted phase transition in the two-phase-like region, which could be a key factor for the better performances of nanostructured materials.

The two samples will be discussed separately, due to their different cycling behaviour. The monoclinic polymorph clearly shows the trend predicted by the aforementioned DFT calculations, with a lattice expansion, followed by a contraction due to the symmetrisation of the octahedra, and another expansion of the symmetrised structure. The volume expansion at the end of the first discharge is +7.38%, due to the combination of the contraction of a (-0.55%) and the expansion of b (+7.05%) and c (+0.80%). It is worth noting that the lattice parameters of monoclinic $\text{Li}_{11}\text{FeNb}_{11}\text{O}_{29}$ are in agreement with the ones found by Pinus et al.¹⁴ for the orthorhombic sample, confirming the crystallographic similarities between the two structures.

The symmetrisation is a displacive phase transition: the atoms slightly shift, retaining the symmetry of the crystal. The contraction of the lattice parameters is mainly due to the sliding of Nb atoms along the shear planes, that is associated with the symmetrisation of the M-O cages.

The symmetrisation of the octahedra starts at around half of the maximum lithiation available ($x = 12$) and takes a couple hours to be complete at C/10. Due to the micron-size of the particles of the active material, a high first cycle irreversibility is detected, involving almost half of the intercalated Li^+ ions (Fig. S4). This seems a proof that a portion of the Li sites are quite irreversible (at least in micron-sized samples). During charge, the reversible half of Li sites is extracted, with a new distortion of the M-O octahedra inferred from the trend of lattice parameters. In the following cycle of discharge and charge, the lattice parameters perform a sort of loop around the values corresponding to the symmetrisation.

The orthorhombic sample instead does not seem to undergo the symmetrisation during the first discharge, where it only expands ($a + 0.25\%$, $b + 1.11\%$, $c + 1.27\%$). The lattice parameters at the end of the first discharge do not even match the ones found from Pinus et al.¹⁴. In the following steps, the drop in a and the further increase in the other parameters seem to suggest that the symmetrisation is just delayed in the orthorhombic structure (maybe because of the higher starting symmetry of the pristine structure, already reported).²¹ Again, almost exactly half of the capacity is irreversible, confirming the observations already discussed for the monoclinic polymorph.

As lithium intercalates, the total volume expansion of $\text{FeNb}_{11}\text{O}_{29}$ is mitigated by the contraction within the block plane. The presence and subsequent relaxation of the octahedral distortions provides a mechanism to realise smaller volume changes in this structural family. The tempered volume changes in shear oxides contribute to their observed stability over 1000 cycles even with micrometer-dimension particles.¹⁰

This feature is really beneficial for long-term applications, but one may wonder if this symmetrisation can occur at higher C-rates, where shear oxides shine with their pseudocapacitive features. To this aim, we were able to cycle the cells at a fivefold current ($C/2$), obtaining interesting results (Fig. 3) that are closer to the ones observed by other authors¹⁸: this time both polymorphs seem to undergo the symmetrisation, with a shrinking of the lattice parameters a and c clearly detectable at almost half of the discharge. Also, the hysteresis observed during the charge is reduced, confirming the increase in the coulombic efficiency already observed in charge-discharge measurements. This seems to suggest that the symmetrisation does not hinder the high-rate performances of this kind of materials. However, the capacity drop already observed in rate capability tests limits the observed capacity at higher C-rates.

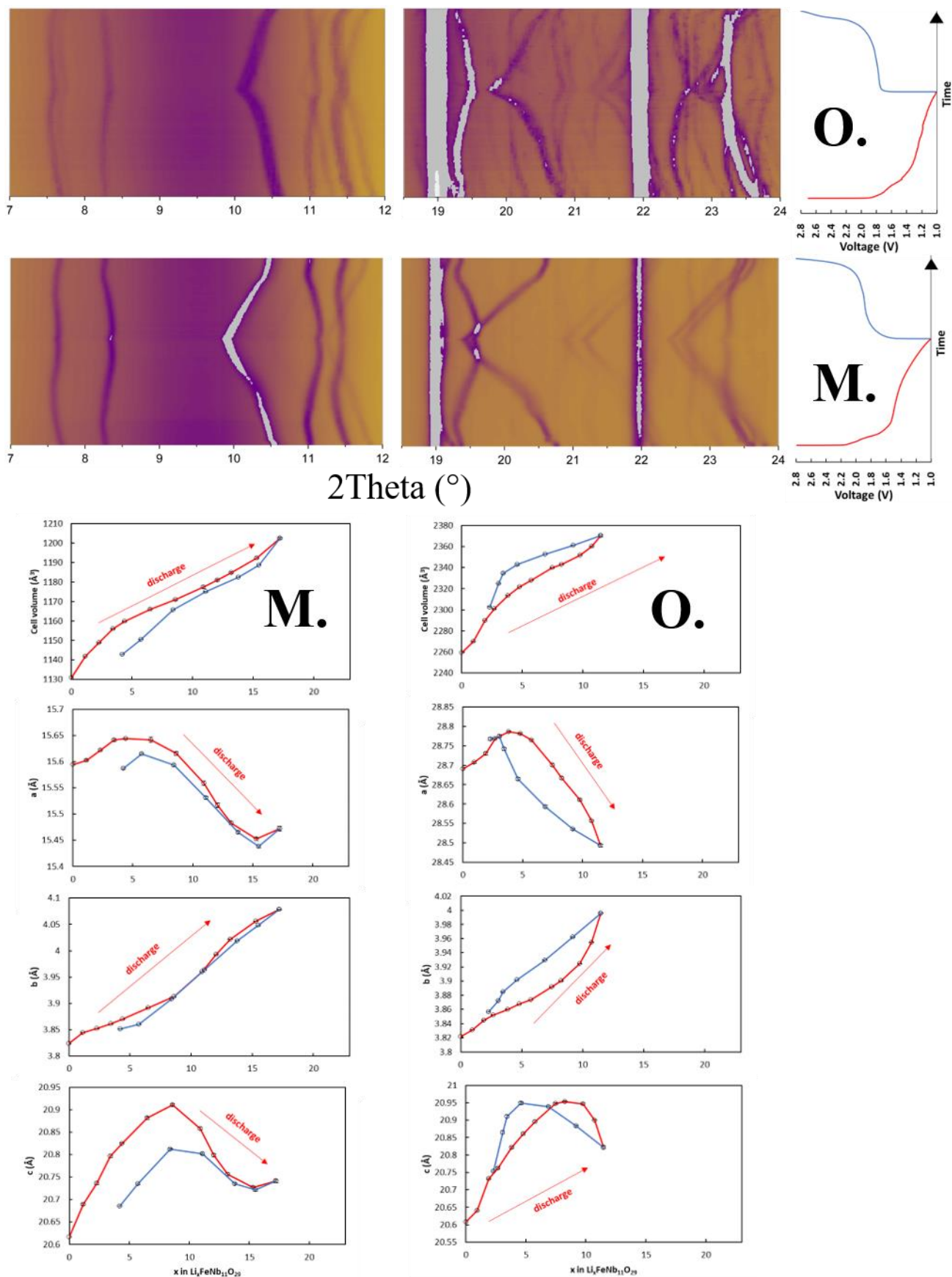


Figure 3 –XRD patterns and refined lattice parameters, for both samples, during *operando* XRD measurements at a higher current (C/2). M. stands for monoclinic and O. stands for orthorhombic.

2.2.2 *In situ* Raman Spectroscopy

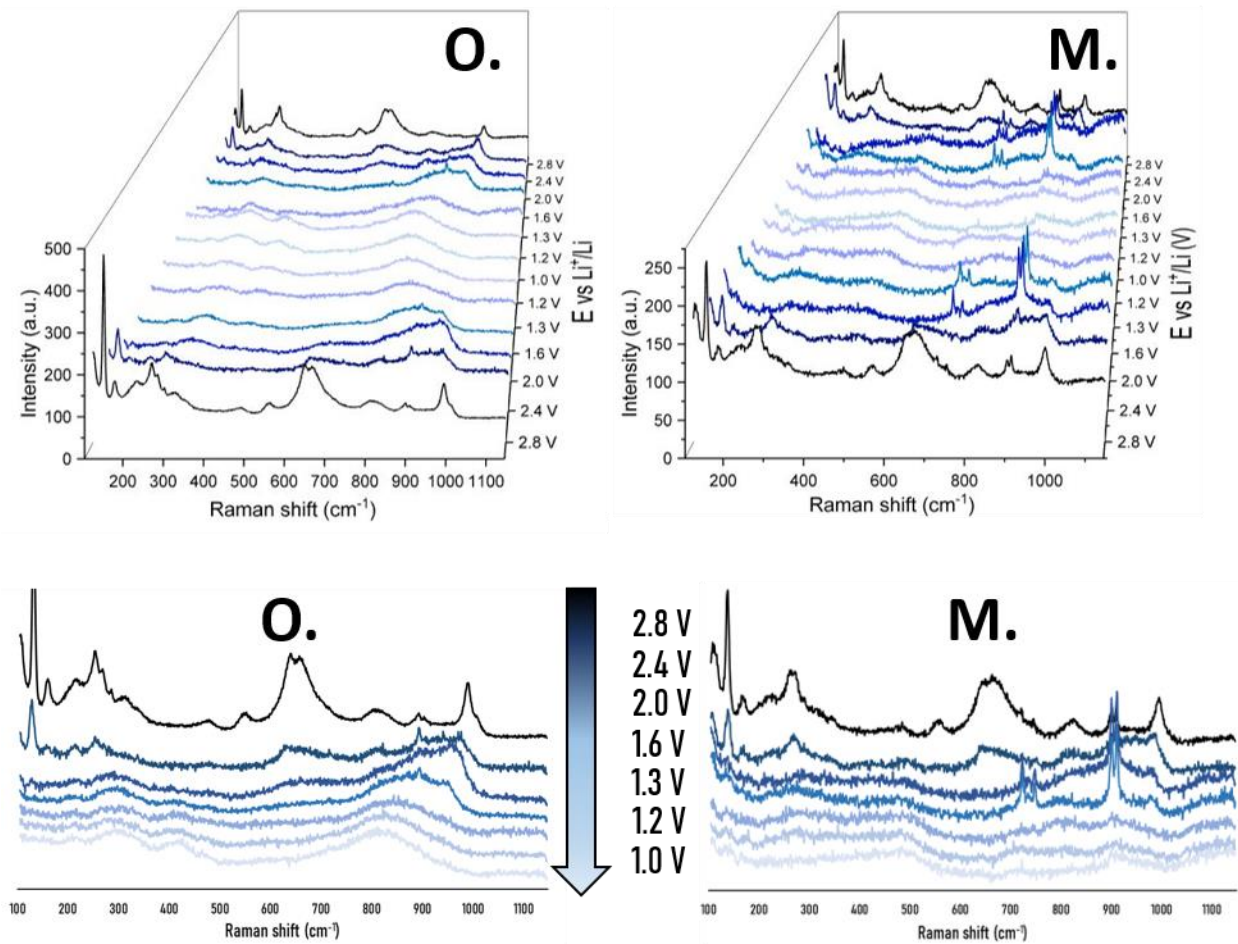


Figure 4 – *in situ* Raman spectra recorded at different potentials, for both the samples.

Raman spectroscopy is very sensitive to the structure and bond order of transition metal oxides, especially in the region of metal-oxygen stretching modes, thus making the technique a very useful tool for *in situ* studies of electrode materials for secondary batteries. Before discussing the spectra, it is useful to mention some Raman experiments on analogous compounds, as reference, because to our knowledge *in situ* Raman experiments on FeNb₁₁O₂₉ were never reported before.

As already mentioned, the structure of FeNb₁₁O₂₉ is often described as ReO₃-like blocks. The rhenium oxide ReO₃ has cubic perovskite-type structure (ABO₃) for which no gerade optic modes are predicted, and no Raman signal is expected. The Raman bands observed in a few papers were attributed to the presence of surface defects that lower the local symmetry.²⁷ The closely related WO₃ can form insertion compounds (the tungsten bronzes A_xWO₃) that are symmetrised when x is closer to 1. Cubic Li_xWO₃, which is similar to ReO₃, does not have Raman-active modes.

²⁸⁻³⁰ During an *in situ* experiment on the electrochromic application of WO₃, Li ions were intercalated into the layers of WO₃: red and blue shifts were detected, alongside the drop/disappearance of some intensities. The frequency shifts were attributed to the lattice parameter variations, while the decrease/vanishing of Raman modes was caused by the higher symmetry of the lithiated phase.³⁰

The spectra of FeNb₁₁O₂₉ will be discussed on the basis of the diatomic approximation, already mentioned in our previous paper.²¹ In brief, the diatomic approximation allows a straightforward interpretation of the Raman spectrum of a crystalline metal oxide compound because it assumes that there are no vibrational interactions between neighboring metal-oxygen bonds in the lattice.³¹ Each metal-oxide polyhedron is reduced to an assembly of metal-oxygen diatomic functionalities, characterized by their own diatomic force constants and reduced masses. The force constant of a metal-oxygen bond has a correlation (approximated by a simple Morse potential energy function) with its interatomic distance. This treatment results in an exponential relation between Raman stretching frequency and bond distance, where the pre-exponential and exponential factors are empirically derived.³¹

Here, we will follow the empirical formulae (Eqn. 1-2) derived from ref.³¹ in order to correlate the frequencies of the Raman modes with their bond distance and valence, according to Pauling's valence sum rule. The valence sum rule states that the sum of the individual Nb-O bond valences, or bond orders, equals the formal oxidation state of the niobium cation, i.e. 5.0 valence units (v.u.) in the case of a Nb⁵⁺.³¹

$$\nu(\text{cm}^{-1}) = 25922 e^{-1.9168R}$$

Equation. 1

$$s(\text{Nb} - \text{O}) = (R/1.907)^{-5}$$

Equation 2

Where ν is the Raman shift corresponding to the stretching of a Nb-O bond with length equal to R Å, s is the bond valency and 1.907 is the estimated bond length for an Nb-O bond with unit valence. 25922 and 1.9168 are the empirically derived pre-exponential and exponential factors. The uncertainty on the the calculated stretching frequency is 30 cm⁻¹.

Not all Raman bands present in the Raman spectrum of a crystalline niobium oxide are assigned to Nb-O diatomic functionalities because some Raman bands are symmetry related. This complication is especially evident in the assignment of the longer Nb-O bonds. The symmetry-related bands result from internal or external modes involving groups of three or more atoms present in the crystal, and these modes are not accounted for in the diatomic approximation. Raman bands arising from symmetry-related modes almost always occur at low frequency, < 300 cm⁻¹, but

seldom occur at high frequencies (molecules confined to a crystalline lattice and possessing a high degree of point-group symmetry).³¹

The series of *in situ*-Raman spectra for both the polymorphs is reported in fig. 4. The reversibility of the intercalation reaction is confirmed by the recovery of the shape of the pristine spectrum after a full cycle of intercalation/deintercalation.

The characteristics bands associated with the vibrational modes of Li–O bonds are located in the low Raman shift region (since Li–O interatomic distances are very large), below the instrumental detection limit ($\leq 80 \text{ cm}^{-1}$).²⁹ The modes deriving from the electrolyte are sometimes detected, depending on the amount of irradiated liquid in each measurement. They can be easily recognized by their sharpness and position, unaffected by the reaction. Their Raman shifts are located at 714, 739, 891 and 901 cm^{-1} , as one can figure out from the comparison between a powder $\text{FeNb}_{11}\text{O}_{29}$ and a $\text{FeNb}_{11}\text{O}_{29}$ particle totally wet with electrolyte, in the electrochemical cell (see Fig. S5). This analysis also serves as a proof that the Raman spectrum of the sample in the the cell in OCV conditions (2.8 V) is identical to the powder sample. Hence we will discuss only the Nb/Fe-O bond vibrations. In OCV conditions, multiple peaks arise in the different regions of the spectrum:

- In the high-frequency region peaks at 990 and 896 cm^{-1} correspond to the stretching modes of very short Nb-O bonds (respectively 1.70 and 1.75 Å), similar to double bonds because of their valence, associated with very distorted edge-sharing NbO_6 octahedra. The peak at 810 cm^{-1} is due to the symmetric stretching mode of collinear Nb-O-Nb bonds (1.80 Å) due to corner-shared octahedra.
- In the middle-frequency region there is most of the activity, given by the intense peaks at 660, 640 cm^{-1} with a shoulder at 550 cm^{-1} (corresponding Nb-O distances of 1.91, 1.93 and 2.01 Å), deriving from symmetric stretching of slightly distorted octahedra. The band at 478 cm^{-1} corresponds to the stretching of a Nb-O bond with length of 2.08 Å.
- In the low-frequency region, where the bending modes are active, multiple bands arise, the most notable one being centered at 130 cm^{-1} .

The spectrum of $\text{LiFeNb}_{11}\text{O}_{29}$ (2.4 V) is quite reminiscent of the pristine phase, with differences appearing in the high- and low-end of the spectrum. The most evident change is given by the loss of intensity and number of peaks, indicating a symmetrisation of the structure. The high-/middle-frequency intensity ratio increase, indicating a distortion during this first phase of lithiation (increasing vibrations of short bonds), confirming the lattice expansion observed with XRD measurements in the first solid-solution region.

The next spectrum, recorded at 2 V vs Li^+ , is already typical of a high-symmetry phase, with few broad bands. The shape of lower-potential spectra is maintained, but some blue and red shifts prove that the symmetrised structure is being distorted, as already observed with XRD in the second solid solution region. For these high-symmetry phases the diatomic approximation and the empirical formulae do not apply, as the experimental data show: most of the Raman activity is centered at high wavenumbers ($800\text{-}900\text{ cm}^{-1}$) that should correspond to very short bonds ($< 1.8\text{ \AA}$), while in the lithiated phases average bond lengths fall in a limited range from 2 to 2.1 \AA .¹⁴

The explanation resides in the aforementioned symmetry-related bands (that are not accounted for in the diatomic approximation) that occur at high frequencies for highly symmetric groups of atoms.

However, the trend is significant: at the potential corresponding to the symmetrisation (1.6 V), this Raman activity shifts to higher wavenumbers, because bond lengths decrease due to the lattice shrinking. After the symmetrisation, bonds are elongated due to the expansion of the symmetrised structure, but also due to the redox reactions involving Nb cations (lower-valence Nb cations will have longer bonds because of the Pauli sum valence rule).

During the charge, the Raman activity is fully recovered, proving the structural stability of the host framework.

2.3 The origin of symmetry: coordination environment

The coordination environment of cations holds a relevant role for the functional properties of every kind of material. For electrode materials, in order to have a better understanding of the structural changes upon lithiation, both the coordination of lithium and transition metal cations have to be taken into account.

2.3.1 Transition metals

When talking about d^0 cations-containing structures, the 2nd order Jahn-Teller effect must be introduced: the energy of empty d orbitals is lowered as the cation becomes smaller and more charged. If the energy is lowered sufficiently, the empty d orbitals are able to mix with the filled p orbitals of the ligands. In extended structures this leads to a number of different electronic configurations with closely spaced energies. Any degeneracy in these configurations can be removed by a spontaneous distortion.³² Any lowering of the electronic energy caused by distortion has to compete with a possible increase in the structural energy (the principle of maximum symmetry is expected to work against distortions). The magnitude of this electronic effect depends inversely on the size of the energy gap between HOMO and LUMO. LUMO has cation d character, and is lowered in cations with higher charge and smaller size. Sc^{3+} and Zr^{4+} are dominated by

structural energy, showing no tendency to distort, while V^{5+} and Mo^{6+} are dominated by electronic energy, and thus always distorted. In between lie Ti^{4+} , Ta^{5+} and Nb^{5+} , which are sometimes distorted, depending on the nature of structural energy.³²

When 2 coordination octahedra share edges or faces, as in Niobium shear structures, the cations are brought into contact and tend to relax by moving away from each other, making distortions possible. The size of the cation-cation repulsion is important in determining the direction of the J-T distortion, not its magnitude.³² For $FeNb_{11}O_{29}$, it was already observed that different crystallographic sites possess different distortion degrees. The 6th site at the center of the building blocks (See Fig. 5), exclusively corner-sharing, is the less distorted because the Nb cations are far away from each other, while sites 1, 2 and 3 are more distorted than sites 4 and 5 because of the larger amount of shearing along the shorter side of the building blocks.²¹

In the lithiated phase ($Li_xFeNb_{11}O_{29}$), the Jahn-Teller effect, together with the repulsive force between Nb and Li cations and the increased ionic radius of the cations (in high-spin octahedral coordination: $Nb^{5+/4+/3+} = 0.64\text{\AA} \rightarrow 0.68\text{\AA} \rightarrow 0.72\text{\AA}$; $Fe^{3+/2+} = 0.645\text{\AA} \rightarrow 0.78\text{\AA}$)³³ is responsible for the cell expansion. One of the main causes of the structural stability of the iron niobate is thought to be transition from the 2nd to 1st order J-T distortion of NbO_6 octahedra: while the d^0 (Nb^{5+}) octahedra are heavily distorted, both the d^1 and d^2 (Nb^{4+} and Nb^{3+}) are weakly distorted, because the degeneracy of electronic configurations is limited to the T_{2g} set of orbitals, not pointing towards ligands. There was already experimental proof of the different coordination environments experienced by d^0 and d^1 NbO_6 octahedra in such a structure.^{14,34}

The reduction of d^0 cations prone to second-order Jahn-Teller (SOJT) distortions usually leads to a removal of the distortion. In shear oxides, the reduction can alleviate both the SOJT distortions as well as the electrostatic repulsion between cations along the shear planes, inducing symmetrisation.

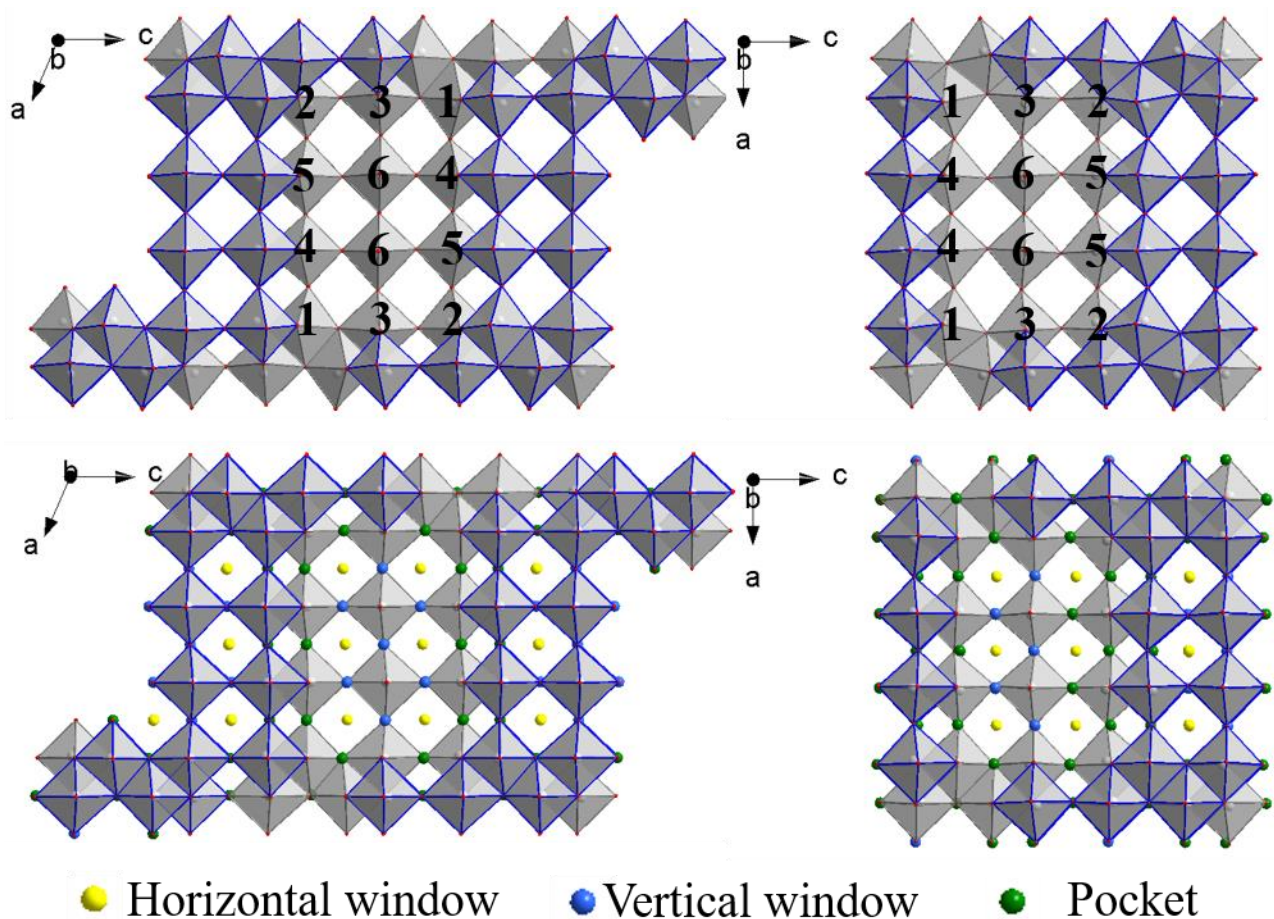


Figure 5 – Coordination environment of Nb⁵⁺ in FeNb₁₁O₂₉ (above) and Li⁺ ions in Li₂₃FeNb₁₁O₂₉ (down), in the monoclinic (left) and orthorhombic structures (right). Different kind of Li sites are highlighted with different colours.

2.3.2 Lithium ions

Previously, most attempts devoted to explain the lithium insertion mechanism in block-type phases have referred to the types of cavities that are found in shear structures, which were first identified by Cava et al.³⁵ The DFT calculations do not support this type of mechanism; each cavity is associated with multiple lithium sites. Instead, it is more accurate to describe the lithium insertion mechanism by the type of site (window, pocket) that is being filled, and what structural changes this lithium occupation causes. The cavity types are very useful however for the structural understanding of pristine shear phases.¹⁰

Lithium sites in block-type structures (deduced by neutron diffraction studies for lithiated block-type structures TiNb₂O₇ and H-Nb₂O₅)^{36,37} are divided into three sets; fivefold coordinated 'pocket' sites at the edge of the block, fourfold coordinated horizontal window positions, and four-

fold coordinated vertical 'window' positions (Fig. 5). Horizontal window positions have a symmetric arrangement of oxygen atoms, while vertical window positions and some of the pocket sites are less symmetric. The insertion into fivefold coordinated sites is energetically more favourable, while insertion into vertical window positions is the least favourable because these sites are too large for fourfold coordination of lithium by the oxygen atoms. The single site energies of around -2.1 eV agree well with the starting point of voltage profiles at 2 V vs. Li⁺/Li.¹⁰ In 2014 Pinus already reported the 5-fold- and 4-fold-coordinated Lithium sites in FeNb₁₁O₂₉, suggesting that entropic and/or kinetic factors play an important role in driving Li atoms into the available sites during the insertion reaction, making the attribution of the lithiation sites even harder.¹⁴

Following the works of previous authors^{10,14}, the structural models of the lithiated FeNb₁₁O₂₉ were deduced, on the basis of our previous CV results²²: in Li₁₂FeNb₁₁O₂₉ (corresponding to Li₁₂Fe²⁺₁₁Nb⁴⁺₁₁O₂₉, which is considered the symmetrised phase), all pocket sites were fully occupied, while the remaining 2 Li/f.u. were placed on the other sites with equal amounts.

In the orthorhombic polymorph, there are five 4c sites and nine 8f sites available for Li insertion. In the fully lithiated niobate, the amount of Li/f.u. is 23 (5*1 Li/4c + 9*2 Li/8f), while in the symmetrised phase the amount is 12, corresponding to a unitary occupancy of the six pocket sites (two 4c and four 8f, equal to 10 Li/f.u.) and an equidistribution of the remaining Li ions on the other sites (2/13).

In the monoclinic polymorph, there are one 2c site and eleven 4i sites, corresponding to 2*1 Li/2c + 11*2 Li/4i ions f.u. in the fully lithiated niobate. In this case the pocket sites are five 4i sites, and the residual occupancy is 2/13 for every other site.

Both the maximum amount of Li ions accommodated in the host lattice and the number of reactive electrons is 23, corresponding to a theoretical capacity of 400 mAh/g. However, the theoretical capacity of bare window sites falls down to 226 mAh/g.

2.4 The pseudocapacitive features of FeNb₁₁O₂₉

While most of the materials employed in LIBs store charge through solid-state diffusion, few transition metal oxides exhibit a relatively new property (the first materials were identified in the 1970's) termed pseudocapacitance: a material is said to be pseudocapacitive when reversible redox reactions occur at (or near) the surface of a material in contact with an electrolyte, or when these reactions are not limited by solid-state ion diffusion. This feature leads to high energy density at high charge–discharge rates, and can be an intrinsic or extrinsic property to the material.

Extrinsic materials do not exhibit pseudocapacitance in the bulk state due to phase transformations during ion storage. With these materials, increasing the surface area through nanostructuring leads to improved high-rate behavior due to a decrease in diffusion distances and in some cases, the suppression of a phase transformation.³⁸

The pseudocapacitive features of FeNb₁₁O₂₉ are known since few years ago.^{17,18,22} It shows intrinsic pseudocapacitance which is termed intercalation pseudocapacitance, which occurs when ions intercalate into the tunnels or layers of a redox-active material accompanied by a faradaic charge-transfer with no crystallographic phase change. The absence of a two-phase equilibrium can be observed in the sloping potential profiles already reported in literature.²² Also DFT calculations on analogous compounds indicated the presence of stable or nearly stable phases for each of the intermediate lithiated phases, excluding the possibility for two-phase regions.¹⁰ The flatter region of the voltage profile of FeNb₁₁O₂₉ corresponds to a displacive phase transition, that is not a two-phase equilibrium, because it does not involve breaking of bonds or nucleation and growth of new phases.

2.4.1 Cyclic Voltammetry

In a cyclic voltammetry experiment, the timescale of the experiment is controlled by the sweep rate (v , mV s^{-1}). The current response to an applied sweep rate will vary depending on whether the redox reaction is diffusion-controlled or surface-controlled (capacitive). For a redox reaction limited by semi-infinite linear diffusion, the current response varies with $v^{1/2}$; for a capacitive process, the current varies directly with v . Therefore, for any material the following general relationship may be written for the current at a particular potential:

$$i(V) = k_1 v^{1/2} + k_2 v$$

Solving for the values of k_1 and k_2 at each potential allows for the separation of the diffusion and capacitive currents.³⁸

Another feature of rapid energy storage is the relationship between peak potential and sweep rate. In a capacitive system, there is very little potential hysteresis between the charging and discharging steps particularly for slow charge–discharge times. In a cyclic voltammetry experiment, this translates into a small or no potential difference between the anodic and cathodic peak currents at slow sweep rates. It should be noted that polarization processes will lead to peak voltage separation in all electrochemical systems.³⁸

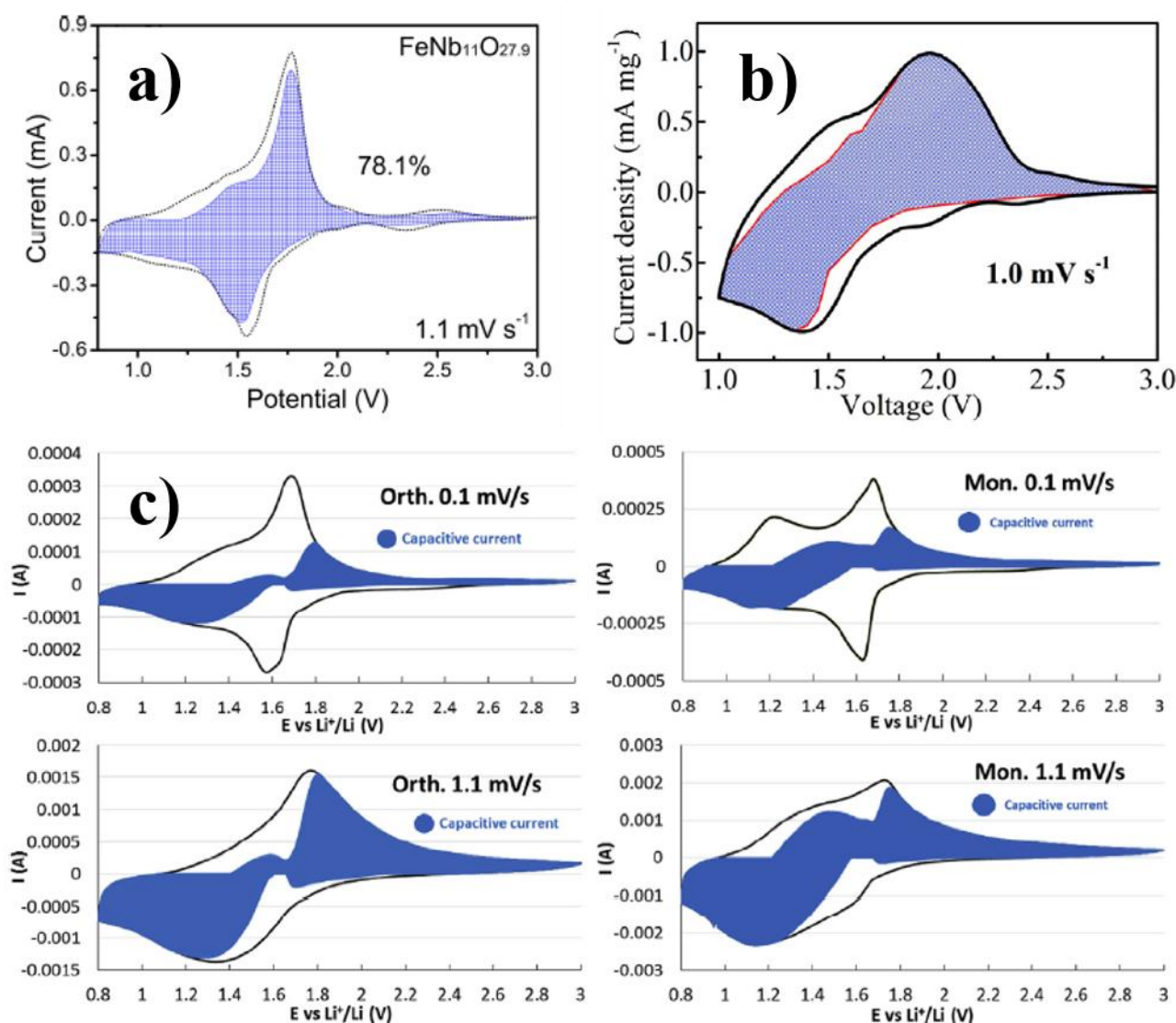


Figure 6 – Voltammograms with pseudocapacitive currents evidenced. Figures reproduced with permission from references ¹⁷ (a - Orthorhombic micron-sized FeNb₁₁O_{27.9}), ¹⁸ (b - Monoclinic nanotubes) and ²² (c - Monoclinic vs Orthorhombic micron-sized)

For FeNb₁₁O₂₉, as for many other materials with pseudocapacitive features, the typical voltammogram shows broad peaks with little differences between the anodic and cathodic branch. Depending on the synthesis (and on doping), the relative amounts of pseudocapacitive and diffusive current can vary: micron-sized particles show larger amount of diffusive current than nano-sized samples. However, the common feature reported by all authors who performed this kind of experiments is a predominantly pseudocapacitive intercalation reaction (up to 80% of the total current at 1 mV/s), with the exception of the main redox peak at 1.6 V (Fig. 6). The main redox peak corresponds to the aforementioned flatter region of the voltage profile, and consequently to the symmetrisation, which is a displacive phase transition. The symmetrisation is

also responsible for most of the potential hysteresis that is recorded between the cathodic and anodic branches, because during the discharge step, Li ions enter the interstitial space of the host lattice and electrons are accepted into the transition metal d orbital, followed by an energy decrease and phase stabilization. However, in reverse, more energy is consumed as ions and electrons must be promoted from the lower energy states. In particular, the energy spent during charge is slightly higher than that delivered during discharge. This energy difference is the source of the potential gap between the charge and discharge curves, or in this case between the two branches of the voltammogram.³⁹

Fig. 7 shows the voltammograms obtained with a sweep rate of 0.01 mV/s (1/10th of the usual slowest sweep rate found in literature) for both the polymorphs of the iron niobate. Peaks are still overlapping, because the multitude of possible sets of cation-cation neighbours deriving from the cationic disorder produces a distribution of site energies instead of single values, causing the peak broadening. However, the resolution coming from the slow sweep rate allows the certain attribution of previously undefinable phenomena.

The peak around 2.5 V can easily be assigned to the $\text{Fe}^{3+/2+}$ redox couple: in other isostructural materials with an electrochemically inactive transition metal ($\text{GaNb}_{11}\text{O}_{29}$ or $\text{AlNb}_{11}\text{O}_{29}$) that peak does not appear.^{40,41} Further, the electrochemical potential of electrodes increases with the number of electrons in d orbitals of transition metal elements of the same period: the electrons in the outer shell are more strongly attracted by atomic nuclei, resulting in higher energy consumption or release during electron transfer. Similarly, if the period increases in the same family, the binding energy of electrons and the electrochemical potentials of cathodes decrease, as the nuclei not as strongly attracted to the 4d electrons as they are to the 3d electrons. As weaker attraction corresponds to a lower energy for electron transfer, the corresponding materials have a lower potential.³⁹ All the other peaks below 2 V are then assigned to the $\text{Nb}^{5+/4+}$ ($E \geq 1.6$ V) and $\text{Nb}^{4+/3+}$ ($E < 1.6$) redox couples. The shape of the voltammogram suggests more than one peak per redox couple. In order to discuss a possible correlation between peaks and Li insertion sites, we have to mention that different positions possess different site energies and produce different potentials when ions are inserted into or extracted from host materials. The lower the site energy in a crystal lattice, the more external energy is consumed to transfer one ion from the occupied site to a free state.³⁹ DFT calculations suggested that fivefold-coordinated sites are more energetically favourable than vertical window positions, hence the electrochemical potential of “pocket” sites is expected to be higher than vertical window sites. Further, the current detected in CV experiments is pseudocapacitive when Li^+ ions intercalate in the tunnels with no diffusion limitations: hence the sites involved in pseudocapacitive reactions are the window positions

(corresponding to perovskitic cavities), with weaker coordinative bonds. By contrast, the diffusive intercalation should correspond to the 5-fold coordinated lithium sites, more stable.

The broad peaks above 1.65 V are more or less pseudocapacitive,^{16–18,22} with horizontal window positions involved. The multiple set of peaks involving Nb⁵⁺ reduction is likely caused by the different distortion degrees of different horizontal window sites, with possible contribution from pocket sites (the diffusive contribution).

The main redox peak involves the Nb⁵⁺/Nb⁴⁺ redox couple with insertion of Li⁺ ions in pocket sites, which are both symmetric and distorted, giving a splitting which is detectable only at slow sweep rates. This reaction is associated with the symmetrisation of the block, that makes previously distorted vertical window positions available. The main peaks are much sharper than any other peak, because they are associated with a phase transition, while the site energy associated with the other redox events is changing rapidly, due to the lattice expansion. The further reduction of Nb ions (Nb⁴⁺/Nb³⁺) is again pseudocapacitive, meaning that window positions are still involved (both the remaining horizontal and the freshly available vertical).

The reverse process is not exactly identical, as suggested by the analysis of the pseudocapacitive contribution in our previous paper.²² This time the first oxidation (Nb³⁺/Nb⁴⁺) is diffusive, suggesting pocket sites are the first left by Li⁺ ions. Pocket sites are involved until the main anodic redox peak, with a pseudocapacitive contribution in between suggesting that also some window sites are now free from Li⁺ ions.

The little differences between the polymorphs that are detected in the voltammograms can be ascribed to both the different links between the structural blocks and to the different distortion degrees of the structural octahedra: the monoclinic polymorph usually shows a higher and broader redox peak for the Nb⁴⁺/Nb³⁺ which, at higher sweep rates, prevails over the redox peak Nb⁵⁺/4+, because of the faster kinetics associated with pseudocapacitive reactions.

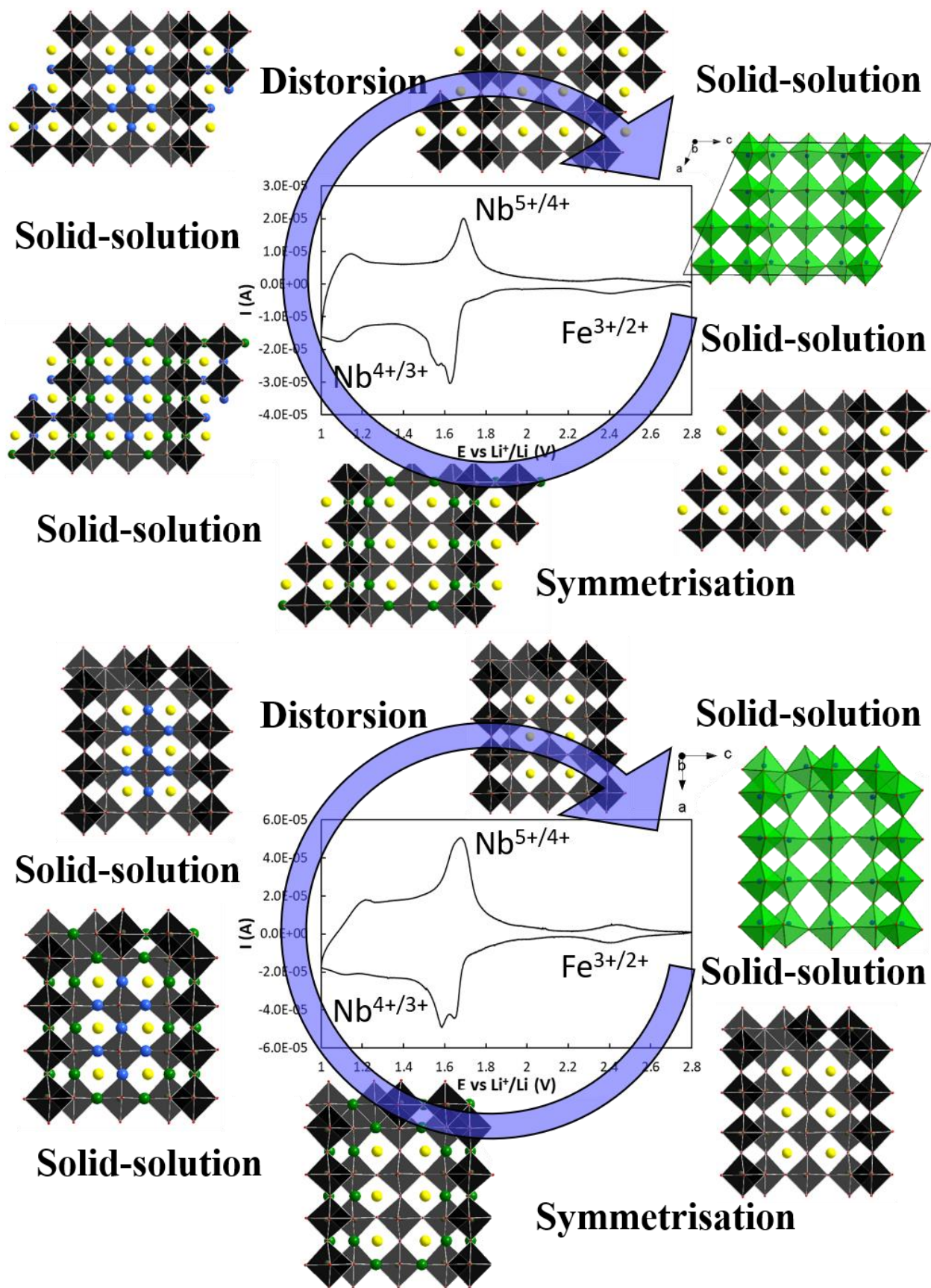


Figure 7 – Voltammograms of monoclinic (above) and orthorhombic (down) FeNb₁₁O₂₉. The lithiation sites are shown with the same colours as in the previous picture (yellow = horizontal

window, blue = vertical window, green = pocket). The pristine phase is green and the lithiated phases are black.

2.4.2 Galvanostatic Cycling with Potential Limitations

2.4.2.1 Rate capability and long-term stability

At the characterization stage, it is important to perform both rate capability tests (in order to check the behaviour of the electrode material at different C-rates) and long-term stability tests, which are the most important for practical applications.

In 2014, Pinus ¹⁴ did not evidence the pseudocapacitive features of the iron niobate, because the C-rates that were chosen for the rate capability test ranged from C/25 to C/2.5.

In 2017, Lou ¹⁵ performed the first rate capability test on FeNb₁₁O₂₉, from 0.1C to 10C. Alongside those positive results, the first long-term stability test was also performed at 10C for 500 cycles, obtaining promising results especially for the Cr-doped sample (Fig. 8).

Since then, different authors performed similar tests, on both polymorphs, obtaining growing results, trying out different dopant ions ^{16,22} or oxygen vacancies ¹⁷ in order to enhance the performance. Doping with other transition metals and nanostructuration ¹⁸ always increased remarkably the structural stability. The 1st cycle coulombic efficiencies reach 90%, with 0.0123% capacity decay per cycle, over 2000 cycles. Zheng et al ¹⁸ also tested FeNb₁₁O₂₉ in full cells with different cathode materials, demonstrating the applicability of FeNb₁₁O₂₉ nanotubes as electrode materials.

It is worth noting that all authors obtained performance that can confirm our previous hypothesis on pocket Li sites: at slow C-rates performances close to 400 mAh/g are obtained because those sites can be occupied thanks to solid-state diffusion and the capacity retention is worse because Li insertion in those sites is not fully reversible.

At higher C-rates, up to 10C, only window sites are suitable for Li intercalation, preventing the capacity from exceeding 226 mAh/g, and allowing the capacity retention to reach higher values.

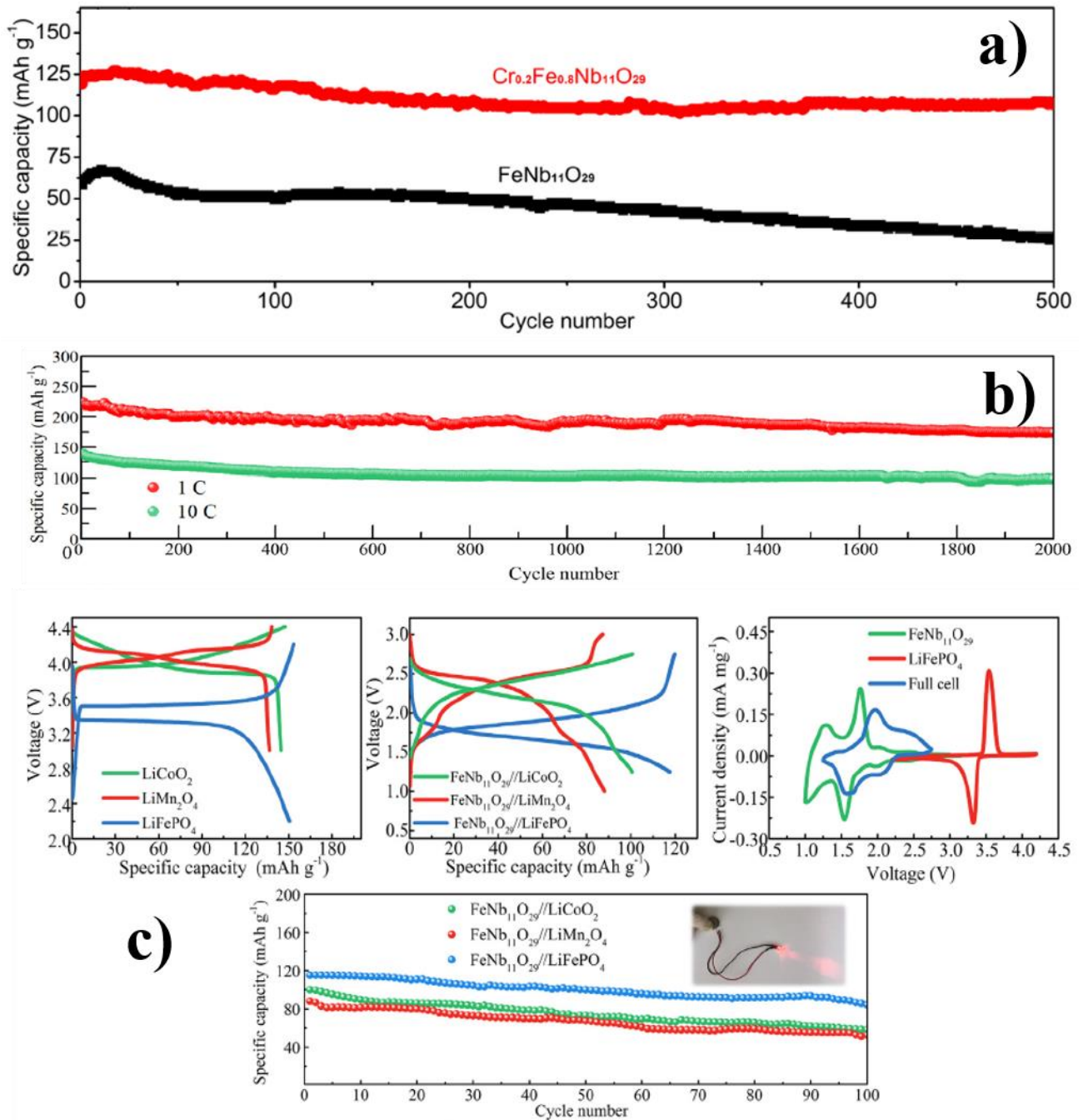


Figure 8 – Long-term stability tests obtained by different authors on half-cells and full cells.

Reproduced with permission from reference ¹⁵ (a – 10C on orthorhombic micron-sized Cr_{0.2}FeNb₁₁O₂₉) and ¹⁸ (b – 1C and 10C on FeNb₁₁O₂₉ nanotubes and c – 1C on full cells with established cathode materials)

2.4.2.2 Voltage profiles

In a constant current experiment, pseudocapacitance is indicated by a small voltage hysteresis between the charging and discharging steps. Since these materials do not undergo a phase transformation, the profile of potential vs. capacity will be almost linear in shape.³⁸

The voltage profile of $\text{FeNb}_{11}\text{O}_{29}$, as already mentioned, is almost linear but with 3 different slopes (Fig. 9): at high and low potentials sloping curves are reported, with sometimes also a small flat region at 2.4 V (corresponding to the $\text{Fe}^{3+}/\text{Fe}^{2+}$ redox couple). In between, a flatter region corresponding to the main redox peak and to the displacive phase transition.

Sloping regions are characterized by lattice expansion, that actually changes the free energy of Li insertion sites. The two-phase-like region is flatter because the expansion is mitigated by the shrinking in the block plane that causes the free energy associated with the intercalation of Li ions to stay almost constant for a quite large amount of time (and capacity).

Increasing the C-rate causes the all slopes to increase, retaining the split at ca. 1.6 V. Voltage hystereses are very limited, as predicted for pseudocapacitive materials.

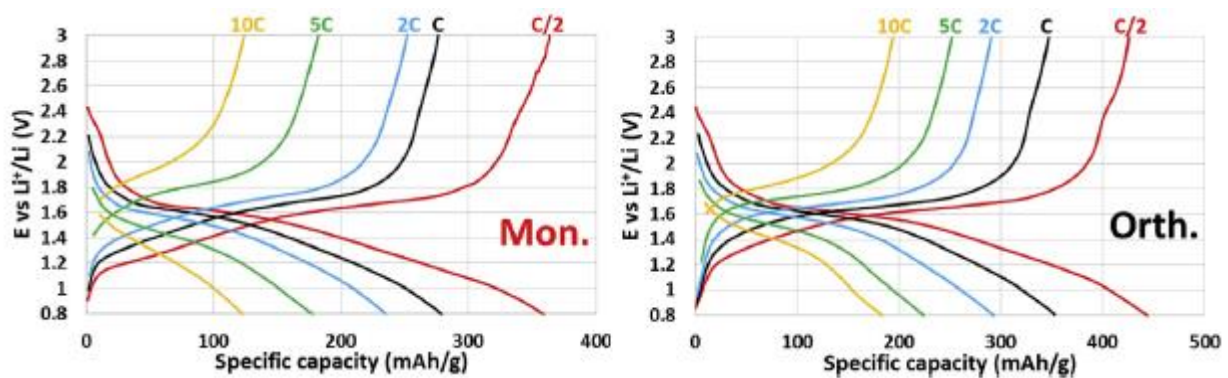


Figure 9 – Voltage profiles obtained from rate capability tests on micron-sized Monoclinic and Orthorhombic $\text{FeNb}_{11}\text{O}_{29}$. Reproduced with permission from reference²²

2.4.2.3 Differential capacity

One of the main features proving the pseudocapacitive nature of $\text{FeNb}_{11}\text{O}_{29}$ is the little polarization. Alongside its observation in CV experiments (see figs. 6-7), also galvanostatic cycling can be visualized in an analogous way, thanks to the differential capacity plot (dQ/dV) of GCLP results (fig. 10).

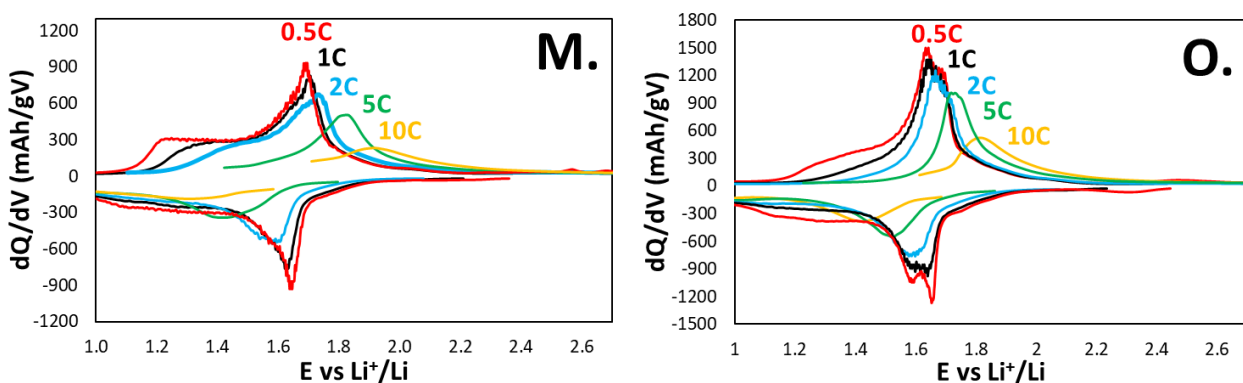


Figure 10 – Differential capacity plot of galvanostatic rate capability test results, for both samples.

The differential capacity plot at 0.5 C shows good correspondance with other CV curves: after very little redox activity in the high-voltage region, the main peak can be located at around 1.6 V. The rest of the graph is characterized by broader peaks, spread all over the lower-voltage region. The peaks at higher C-rates are poorly resolved but still confirm that the material, especially in its orthorhombic form, has very low polarization. This implies that the electrode resistance remains low, which is an essential feature for a material to be employed in advanced LIBs or HEVs.

The peaks of a differential capacity plot correspond to the plateaus in the voltage profile (the narrower the peak, the straightest the voltage plateau). While the overall shape of the curve is affected by thermodynamics of the intercalation, the kinetics of the associated redox reactions affect the evolution of the shape at increasing C-rates.

In a potentiodynamic experiment (such as cyclic voltammetry) the potential is controlled through a reference electrode and the current response has a dependency on the sweep rate. In a galvanostatic experiment, aside from abrupt potential change due to the iR loss, the potential gradually changes because a concentration overpotential is developed as the concentration of the reactant is exhausted at the electrode surface. If the current is larger than the limiting current, the required flux for the current cannot be provided by the diffusion process and, therefore, the electrode potential rapidly rises until it reaches the electrode potential of the next available reaction, and so on. ⁴²

The evolution of the shape of the curves in fig. 10 can be explained on the basis of the cyclic voltammetry: the Nb^{5+}/Nb^{4+} reduction was determined to be mostly diffusive (slower kinetics), while most of the Nb^{4+}/β^{+} reduction was determined to be pseudocapacitive (faster kinetics). This trend was almost reversed during the anodic scan, with significant pseudocapacitive contributions to the Nb^{4+}/Nb^{5+} oxidation. The concentration overpotential associated with the slower diffusive reactions leads to a significant decrease of the intensity, as well as polarization (see the negative peak at 1.6 V), while faster pseudocapacitive reactions are much less affected by increasing the C-rate, preserving most of their intensity and their position (lower-voltage region of the negative branch).

2.4.3 Electrochemical Impedance Spectroscopy

AC impedance can also be used to determine whether pseudocapacitive behavior is taking place. The Nyquist plot for an ideal capacitor is a vertical line, indicating a 90° phase angle. Deviation

from a vertical line to phase angles of $<90^\circ$ often occurs and can indicate pseudocapacitive behavior, which is often represented by a constant-phase element in the equivalent circuit.³⁸

A series of spectra was collected applying different potentials to the $\text{FeNb}_{11}\text{O}_{29}/\text{Li}$ cell (fig. 11) and allowing the cell to reach steady state conditions at each potential, before applying the excitation voltage pulses. For better clarity, both the Bode and Nyquist plots are shown, indicating respectively, the evolution of the shape of the spectra and the values of the resistances.

The pseudocapacitive nature of $\text{FeNb}_{11}\text{O}_{29}$ is evident: the continuous change in the oxidation states corresponding to the entrance/exit of Li^+ ions in/from the structure finds a correspondance in the spectra, that at every potential (apart from high-end potentials where the overpotentials are too high for an ionic charge-transfer resistance) consist of a solution resistance (R_s), 2 charge transfer resistances (R_e and R_i , the first being electronic and the second ionic) and the mass transport, more or less detectable. An analogous model was reported for similar Niobium oxides.⁴³

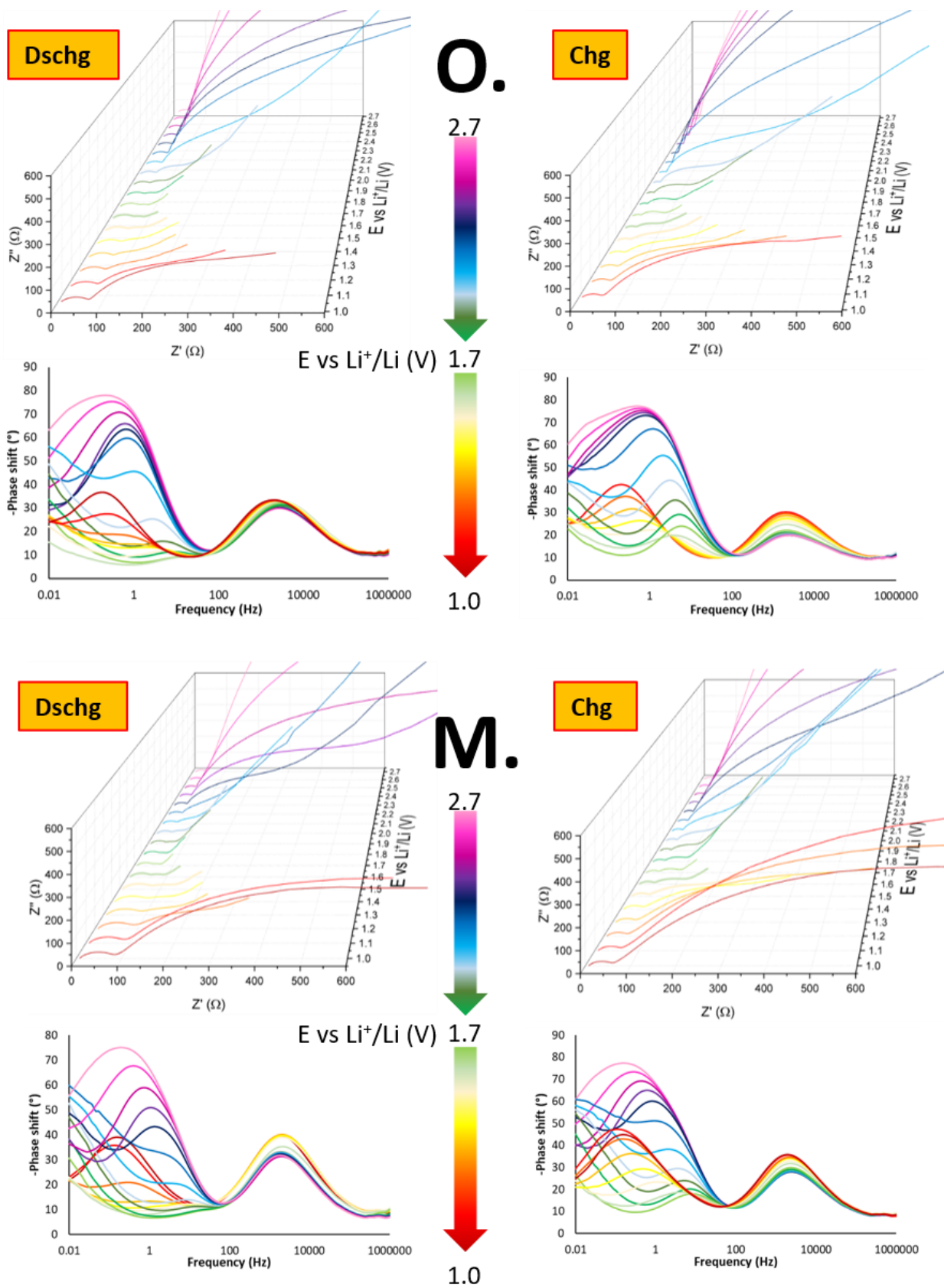


Figure 11 – Nyquist and Bode phase plots of the EIS results, for both the samples.

The evolution of the shape of the spectra shown with the Bode phase plot is representative of the process: the electrolyte resistance (at the high-end frequency of the spectra) is almost constant, indicating the good stability of the commercial electrolyte in the selected potential window. At high frequencies (approx 10^3 Hz) the electronic charge transfer resistance is not much affected by the reaction, for what concerns the frequency of the process. The phase shift instead is slightly higher at the low-end potentials, indicating an increase in the capacitive contribution and thus a non-negligible contribution of the active material to the electron conduction. Due to the unexpected trend observed from the experimental data, the predicted behavior of shear Nb oxides must be introduced.

The coexistence of localised and delocalised states in this kind of structures was reported, because of its implications in the magnetic properties of $\text{Nb}_{12}\text{O}_{29}$ (metallic antiferromagnet).²⁴ In most niobium oxides, wide band-gap insulators, the strong d-orbital overlap along the shear planes gives rise to large bandwidths, and in fact, the delocalised states are hosted on transition metal sites at the block periphery. The preferred electron transport direction is expected to be perpendicular to the block plane. The localised state formed upon lithiation is spread over multiple (predominantly block-central) sites and lies in the plane of the block, with no strong coupling between the lithium ion and the electron. Lithiation/n-doping introduces electrons into the almost empty conduction band and should fully fill the flat band, and also partially fill the remaining dispersive conduction bands, resulting in metallicity (progressively stronger as the phase gets more lithiated), beneficial for high-rate battery performance, and possible electrochromic applications.¹⁰ The change in the colour of the material from green to black was already reported by Pinus.¹⁴ $\text{FeNb}_{11}\text{O}_{29}$ is already slightly conductive (because of Fe^{3+} d electrons), and becomes progressively more conductive as the reaction proceeds: more and more electrons are promoted in the 4d Nb conduction band during the intercalation reaction



The experimental data instead show a the opposite trend: the resistance and the phase shift increase below 1.6 V, i.e. when diamagnetic Nb^{5+} cations are reduced. Our hypothesis is that the increase in R_e can be ascribed to the expansion of the lattice parameter b (perpendicular to the block plane), that decreases the orbital overlapping and the electron transport along the favoured direction.

The ionic charge transfer instead shows consistent changes in the frequency of the process and in the phase shift. At higher potentials, the mass transport dominates the low-frequency region of the spectra. When the overpotentials associated with ionic charge transfer reactions (i.e. the already mentioned redox peaks) are progressively lowered, the low-frequency part of the spectra is a mix of mass transport and ionic charge transfer resistance. The capacitive resistance

corresponding to the ionic charge transfer shows higher capacitive contribution (manifested as higher phase shifts, up to 70-80°) at high- and low-end potentials. The smallest phase shift (quite close to a pure resistance, that ideally has no phase shift) is obtained in correspondance of the highest redox peak (1.6 V), which showed maximum diffusive contribution in voltammetric analyses.^{16,17,22} The consistent frequency shift (ranging from 10⁻¹ to 10¹ Hz), indicates faster charge transfer at potentials closer to the same redox peak. This is not surprising, because peaks in voltammograms correspond to higher reaction rates, i.e. faster charge transfers.

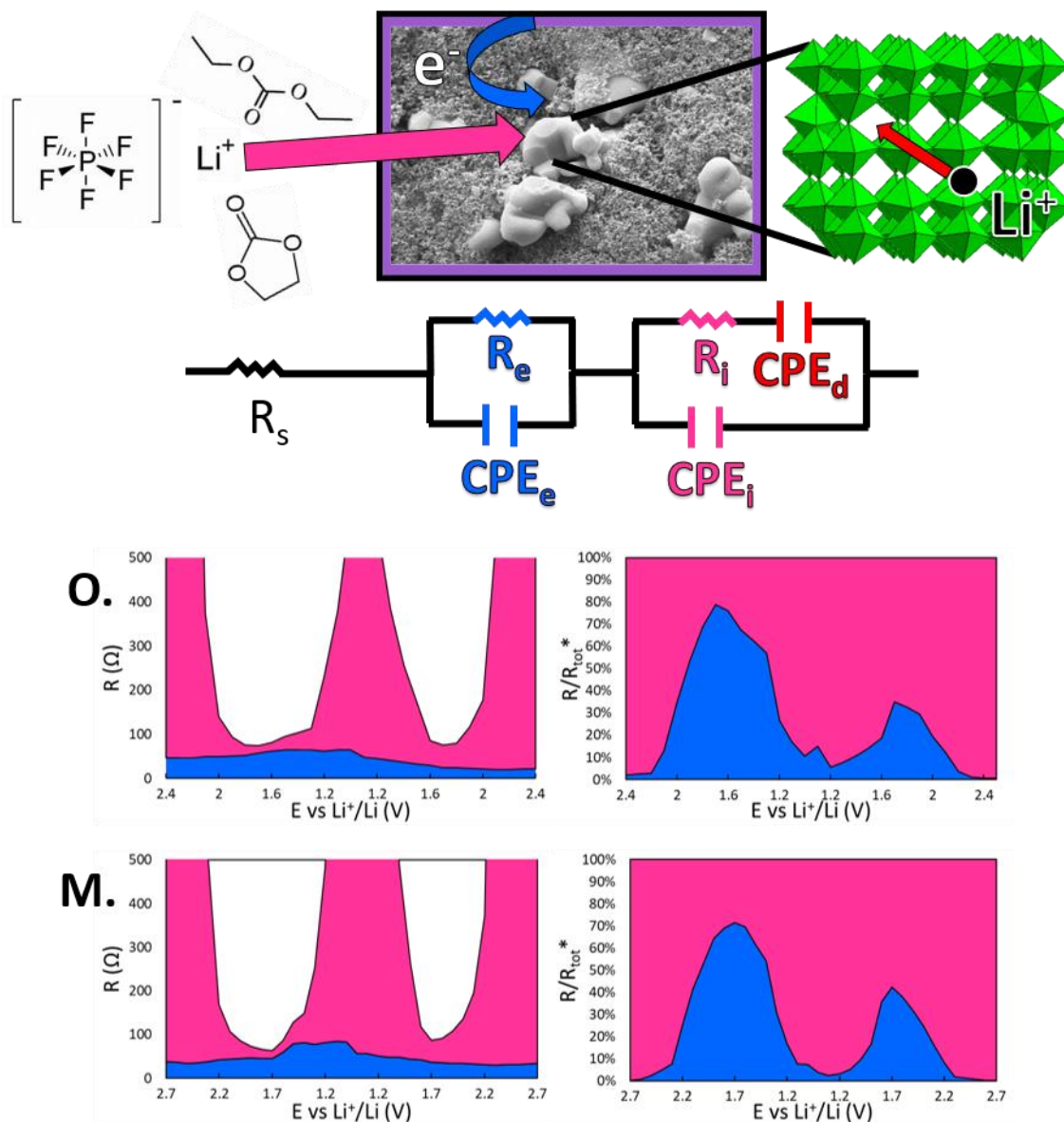


Figure 12 – Equivalent circuit and R vs E plots, for both the samples. Ionic and Electronic resistances are plotted separately on the left and their ratio with their sum (called R_{tot}^*) is plotted on the right.

Of course also the Nyquist plot shows the same trend, with constant and relatively little electrolyte and electronic-transfer resistances, followed by a huge Warburg impedance at higher potentials and a W-shaped trend in the ionic charge-transfer resistance, with a minimum in correspondance of the highest redox peak. The fitted values of the resistances, capacitances and the exponents of the frequency for the Constant Phase Elements (CPE) are reported in Tabs. S6-S7. If we take into account the mathematical formulas employed in the circuit modeling for a conventional solid-state diffusion (Warburg impedance), the exponent of the frequency has a fixed value of 0.5 while for a CPE is variable (Eqn. 3), allowing a rough determination of the pseudocapacitive contribution: the closer the exponent to 1, the higher is the capacitive contribution.

$$Z_{CPE} = 1/[Y_0(i\omega)^N] \quad \text{Equation 3}$$

Where Z_{CPE} is the impedance, Y_0 is constant, ω is the frequency and N a fittable parameter. The determined values (Tab. S6), show a clear trend of pseudocapacitive diffusion at high potentials (N up to 0.95), with an almost solid-state diffusion at lower potentials (N very close to 0.5).

The graphs in fig. 12 clearly show that in the flatter region of the voltage profile (around 1.6 V) the ionic resistance is lower than the electronic one: at 1.7 V the electronic resistance is over 70% of the sum of R_e and R_i (called R_{tot}^*). This serves as a confirmation of the incredible electrochemical properties of niobium shear oxides: the performance obtained with Nb-based electrode materials can be enhanced even more by improving the electron conductivity, because their conduction of Li^+ ions is already surprising. The trend of R_i also suggests that the more symmetrical are the previously called perovskitic cavities, the less resistance they offer to Li^+ solid-state diffusion.

During the charge the trend is similar, with a little hysteresis caused by the aforementioned symmetrisation, manifested with an increase in the internal resistance of the electrode.

2.4.4 Galvanostatic Intermittent Titration Technique

Aside from the determination of the relative amount of solid-state diffusion and pseudocapacitive intercalation, it is very important to study the values of the diffusion coefficient of Li^+ ions into the electrode. One of the most useful techniques to this aim is the Galvanostatic Intermittent Titration Technique (GITT), which consists in a series of current pulses, each followed by a relaxation time. With a GITT procedure, during the pulse, the cell potential increases quickly due to the iR drop and then slowly due to the current pulse (in order to maintain a constant concentration gradient). During the relaxation time the composition of the electrode tends to be

homogeneous through Li⁺ diffusion, resulting in a sudden iR drop followed by a slow potential decrease until steady state conditions. By applying subsequent pulses until the cell is fully charged/discharged the iR drop can be eliminated in the calculation of the diffusion coefficient which, for very short pulse times and small currents, can be expressed as

$$D = \frac{4}{\pi\tau} \left(\frac{n_m V_m}{S} \right)^2 \left(\frac{\Delta E_s}{\Delta E_t} \right)^2$$

Where τ is the duration of the pulse (s), n_m is the number of moles of the host oxide (mol), V_m is its molar volume (cm³/mol) and S the contact area between the electrode and the electrolyte (cm²), while ΔE_s and ΔE_t are two voltage differences (V), related to the steady state voltage change and to the pulse voltage change respectively.⁴⁴

It is worth noting that the diffusion coefficient derived for FeNb₁₁O₂₉ is a true diffusion coefficient, because its solid-solution behaviour implies that the concentration of the intercalant ions changes monotonically as the intercalation proceeds.⁴⁵

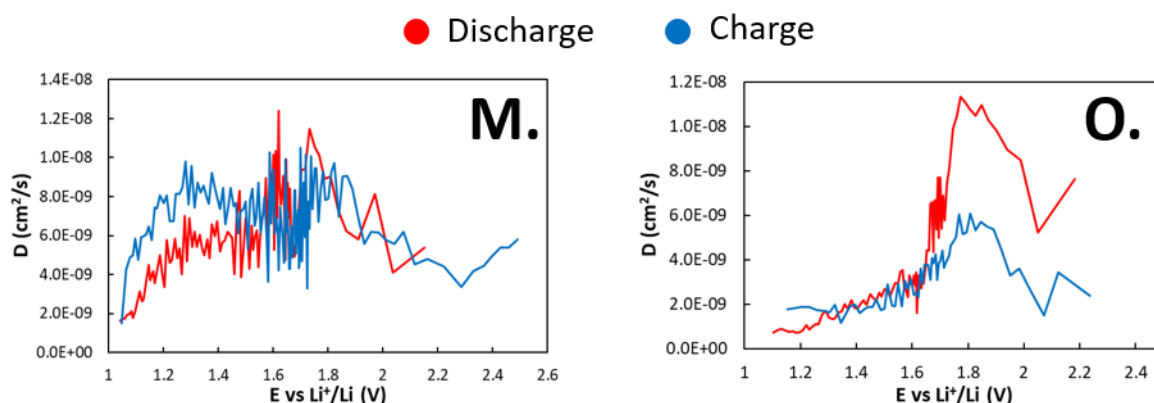


Figure 13 - Diffusion coefficient vs electrochemical potential, for both the samples.

While for phase transition electrode materials a minimum in the values of the diffusion coefficient is observed in correspondance of voltage plateaus/CV peaks (because of the strong attractive interactions between the intercalating species and the host matrix)⁴⁵, FeNb₁₁O₂₉ shows an increase in the values of the diffusion coefficient at some keypoint potentials, likely due to the weak interactions between Li⁺ and the host structure. It has to be precised that with GITT the bare diffusion of Li⁺ ions can be studied, thus excluding the pseudocapacitive contributions that affect the reactions below 1.6 V.

The high-end of the voltage of the D vs E curve (Fig. 13) cannot be studied in detail because of the non-equilibrium conditions of the cell (see the slope of the voltage profile), while in the two-phase-like region the diffusion coefficient shows 2 peaks corresponding to the very first reduction of Nb⁵⁺ cations (approx. 1.8 V) and to the main redox peak (also a Nb⁵⁺ reduction) respectively.

The low-end potential region shows a slower diffusion, with a peak for the monoclinic sample and a flatter shape for the orthorhombic sample. The intercalation reaction at 1.8 V allows very little charge storage when compared to the main redox peak (see figs. 6, 7, 9 and 10), but the corresponding D values are the highest for the Nb⁵⁺ reduction. This suggests that the intercalation involves some entropic factors, with the empty channels being rapidly filled by Li⁺ ions, causing the consistent decline in the diffusion coefficient in the following reactions. Further, another maximum of D is obtained at 1.6-1.7 V, confirming that in the most symmetrical structure the diffusion is really fast.

During charge, a similar trend is observed, with higher values of D at low-end potentials, for which a diffusive de-intercalation was determined in the previously mentioned voltammetric experiments. This suggests again that diffusion is faster in the symmetrical framework.

3. Experimental section

3.1. Sample preparation

Monoclinic and orthorhombic FeNb₁₁O₂₉ (named M. and O. in the whole paper) were prepared by using conventional solid-state syntheses, as described in ref. ²².

The electrodes for conventional electrochemical tests in T-shape home-made Swagelok (and for *operando* XRD measurements) cells were obtained by casting an ink on copper metal. ²²

The self-standing electrodes employed for *in situ* Raman instead were obtained with a modified phase-inversion procedure: ⁴⁶ the ink (50:20:30) was cast onto a porcelain bucket in the shape of a foil, and then covered with distilled water. The phase inversion process causes the initial volatile solvent (NMP) to be replaced by the nonsolvent water, producing a solid porous PVdF structure through precipitation. This thin, flexible electrode limits the need for a metallic current collector as a physical substrate for the slurry, which would hamper *in situ* characterizations.

Both the coated slurries and the self-standing electrodes were then hot pressed, respectively at 90 and 70 °C, and then stored in an Ar-filled glovebox. The electrodes were cut in form of discs (diameter 1 cm), with a mass loading in the range of 1.0-2.5 mg/cm² (for the conventional electrodes) or 5-10 mg/cm² (for the self-standing electrodes).

The Swagelok cells were assembled in a dry box under argon atmosphere (MBraun, O₂ < 1 ppm, H₂O < 1 ppm) using the FeNb₁₁O₂₉-PVdF-C65 electrode as working electrode, Li metal as the reference and counter electrode and a Whatman GF/A disc as the separator, soaked in 1M LiPF₆ in a mixture of ethylene carbonate/ diethylene carbonate (EC/DEC; 1:1 v/v) as the electrolyte (Aldrich).

The pouch cells employed for *in situ* Raman (or *operando* XRD) measurements were assembled in the dry room of DISAT, employing polymer-coated aluminium foil as bag material, nickel strips as current collector and glass (or 50 micron-thick kapton) windows. The working electrode was a 10 (or 15) mm in diameter disc of self-standing (or conventional) FeNb₁₁O₂₉, while Lithium metal served as counter electrode and Whatman GF/A as separator. The electrolyte of choice was again 1M LiPF₆ in a mixture of ethylene carbonate/ diethylene carbonate (EC/DEC; 1:1 v/v). For *in situ* Raman and *operando* XRD measurements, 3D-printed plastic supports were built in order to have better electrical contacts in pouch cells. (Fig. S8)

3.3 Electrochemical measurements

Cyclic Voltammetry (CV) was performed by using an Autolab PGSTAT30 (Eco Chemie) at a scan rate of 0.01 mV/s in the potential range 1.0 - 2.8 V.

Electrochemical Impedance Spectroscopy (EIS) measurements were performed by means of a Frequency Response Analyzer (FRA) Autolab PGSTAT30 (Eco Chemie) apparatus in the frequency range 0.01-10⁶ Hz, with a perturbative sinusoidal wave (amplitude = 30 mV). The spectra were collected in potentiostatic conditions, setting a 2h rest between applying each potential and recording the spectra. The spectra were fitted with the help of the NOVA software.

The Galvanostatic Intermittent Titration Technique (GITT) was performed with an Autolab PGSTAT30 (Eco Chemie) apparatus. Galvanostatic discharge pulses of 10 min with current corresponding to a C-rate of C/20 were followed by 10 minutes of relaxation time, from OCP to 1.0 V and then reversed and applied up to 2.7 V. ⁴⁴

3.4 Combined techniques

In situ Raman measurements were performed with an Autolab PGSTAT30 (Eco Chemie) apparatus at selected meaningful potentials for both charge and discharge, after applying the potential step to the cell and allowing the relaxation current to reach plateau. The measurements were carried out at room temperature using a Labram Dilor spectrometer equipped with an Olympus microscope HS BX40. The 632.8 nm light from a He-Ne laser was employed as the excitation radiation. The samples, mounted on a motorized xy stage, were tested with a 50× objective and with a laser spot of ~2 μm diameter. The spectral resolution was about 1 cm⁻¹. A cooled CCD camera was used as a detector and the typical integration times were about 30 s.

Operando X-Ray Diffraction measurements were performed at the beamline XRD1 of the Italian synchrotron Elettra with the help of a Neware Battery Testing System. Thanks to the 2-D Dectris Pilatus 2M detector (CMOS hybrid-pixel technology operating in single-photon-counting

mode with 3 x 8 modules of Si 320 μm thick, pixel size 172 x 172 μm^2 and a readout time of 3.6 ms, corresponding to a frame rate of 30 Hz) the characterization of the material was time-resolved with great detail. Patterns were collected at 18 keV, both on powder samples in spinned capillaries and on electrochemical cells with Kapton windows during cycles of constant current discharge and charge, at C/10 and C/2. 2D data were integrated after a calibration with LaB₆, thanks to the software Fit2D^{47,48} and then fitted with TOPAS⁴⁹ in order to refine the lattice parameters of the active material.

4. Summary and perspectives

In the recent lithium-ion batteries literature, niobium oxides are attracting growing attention because of their interesting electrochemical properties. This paper added a significant contribution to the research on FeNb₁₁O₂₉, providing a thorough explanation of the intercalation reaction starting from the state of the art and employing *in situ/operando* measurements as well as advanced electrochemical techniques in order to provide greater detail into the correlations between the structural and electrochemical properties of the iron niobate.

The performance-relevant properties of niobium oxides are intimately related to the crystal structure. We demonstrated that the compresence of shear planes delimiting ReO₃-like blocks is the key to the electrochemical performance: the host framework has a great stability because of the shear planes that make the structure less flexible; octahedral distortions are removed through asymmetrisation, alleviating the volume changes and enhancing the already fast Li⁺ conduction in the perovskitic channels typical of the ReO₃-like portion of the structure.

The displacive phase transition that causes the symmetrisation explains the flatter region of the voltage profile observed for many Niobium oxides of the same family: the 2nd order Jahn-Teller effect that causes the Nb⁵⁺O₆ octahedra to be distorted is not present for Nb⁴⁺O₆ octahedra, causing Nb cations on shear planes to slide closer because of the decreased cation-cation repulsion.

The material, as many other M-Nb-O shear oxides, exhibit intrinsic pseudocapacitance, i.e. advantageous kinetic features, even in micron-sized samples. The very weak Li-host matrix interactions are responsible for the high Li⁺ diffusion coefficient. The huge tunnels in the structure provide mass transport that is mostly not limited by solid-state diffusion, showing capacitor-like kinetics. The conduction of Li⁺ ions is so fast, in the symmetrised structure, that the highest charge-transfer resistance in the cell is given by the charge-transfer of electrons.

The main issue for this family of materials remains the electron conductivity but, if tackled with nanostructuration and addition of conductive carbon, high and stable performance can be obtained,

even if at higher C-rates the practical capacity is limited to almost half of the theoretical one because of the solid-state diffusion kinetics of the pocket Li sites.

With this work, we tried to fill the gap on the explanation about the incredible possibilities that FeNb₁₁O₂₉ offers, hoping that the iron niobate will be successfully developed and commercialized in next-generation LIBs aiming at high power density.

Authors contributions

Daniele Spada – Conceptualization, Investigation, Formal Analysis, Visualization, Writing (original draft)

Benedetta Albini – Investigation

Pietro Galinetto – Formal Analysis, Writing (review & editing)

Daniele Versaci – Investigation

Carlotta Francia – Writing (review & editing)

Silvia Bodoardo - Writing (review & editing)

Giorgio Bais – Investigation, Formal Analysis

Marcella Bini – Supervision, Writing (review & editing)

Conflicts of interest

The authors declare no conflict of interest

Acknowledgements

We would like to acknowledge Irene Quinzeni and Usman Zubair for their precious teachings, Mauro Coduri for the fruitful talks and suggestions, Maurizio Polentarutti for the help during the measurements, Alessandro Caserio for the design of the supports for the pouch cells and Lorenzo Airoidi, Riccardo Brucculeri and 3D@unipv lab for the use of 3D printer.

References

- 1 Q. Deng, Y. Fu, C. Zhu and Y. Yu, *Small*, 2019, **1804884**, 1–26.
- 2 Y. Wang and G. Cao, *Adv. Mater.*, 2008, **20**, 2251–2269.
- 3 W. Long, B. Fang, A. Ignaszak, Z. Wu, Y. J. Wang and D. Wilkinson, *Chem. Soc. Rev.*, 2017, **46**, 7176–7190.
- 4 H. Ren, R. Yu, J. Wang, Q. Jin, M. Yang, D. Mao, D. Kisailus, H. Zhao and D. Wang, *Nano Lett.*, 2014, **14**, 6679–6684.
- 5 T. Yuan, Z. Tan, C. Ma, J. Yang, Z. F. Ma and S. Zheng, *Adv. Energy Mater.*, 2017, **7**, 1601625.
- 6 H. Sun, L. Mei, J. Liang, Z. Zhao, C. Lee, H. Fei, M. Ding, J. Lau, M. Li, C. Wang, X. Xu, G. Hao, B. Papandrea, I. Shakir, B. Dunn, Y. Huang and X. Duan, *Science (80-.)*, 2017, **356**, 599–604.
- 7 Y. Ma, H. Chang, M. Zhang and Y. Chen, *Adv. Mater.*, 2015, **27**, 5296–5308.
- 8 S. W. Bokhari, A. H. Siddique, H. Pan, Y. Li, M. Imtiaz, Z. Chen, S. M. Zhu and D. Zhang, *RSC Adv.*, 2017, **7**, 18926–18936.
- 9 B. Zhao, R. Ran, M. Liu and Z. Shao, *Mater. Sci. Eng. R Reports*, 2015, **98**, 1–71.
- 10 C. P. Kocer, K. J. Griffith, C. P. Grey and A. J. Morris, *J. Am. Chem. Soc.*, 2019, **141**, 15121–15134.
- 11 K. J. Griffith, K. M. Wiaderek, G. Cibin, L. E. Marbella and C. P. Grey, *Nature*, 2018, **559**, 556–563.
- 12 L. Yan, X. Rui, G. Chen, W. Xu, G. Zou and H. Luo, *Nanoscale*, 2016, **8**, 8443–8465.
- 13 L. Hu, L. Luo, L. Tang, C. Lin, R. Li and Y. Chen, *J. Mater. Chem. A*, 2018, **6**, 9799–9815.
- 14 I. Pinus, M. Catti, R. Ruffo, M. M. Salamone and C. M. Mari, *Chem. Mater.*, 2014, **26**, 2203–2209.
- 15 X. Lou, Z. Xu, Z. Luo, C. Lin, C. Yang, H. Zhao, P. Zheng, J. Li, N. Wang, Y. Chen and H. Wu, *Electrochim. Acta*, 2017, **245**, 482–488.
- 16 M. Bini, I. Quinzeni and D. Spada, *ChemistrySelect*, 2019, **4**, 5656–5661.
- 17 X. Lou, C. Lin, Q. Luo, J. Zhao, B. Wang, J. Li, Q. Shao, X. Guo, N. Wang and Z. Guo, *ChemElectroChem*, 2017, **4**, 3171–3180.
- 18 R. Zheng, S. Qian, X. Cheng, H. Yu, N. Peng, T. Liu, J. Zhang, M. Xia, H. Zhu and J. Shu, *Nano Energy*, 2019, **58**, 399–409.
- 19 P. Tabero, *Ceram. - Silikàty*, 2005, **49**, 126–131.
- 20 P. Tabero, A. Blonska-Tabero, P. Á. Szilágyi and Z. Homonnay, *J. Phys. Chem. Solids*, 2007, **68**, 1087–1090.

- 21 D. Spada, M. C. Mozzati, B. Albin, P. Galinetto, I. Quinzeni, D. Capsoni and M. Bini, *Dalt. Trans.*, 2018, **47**, 15816–15826.
- 22 D. Spada, I. Quinzeni and M. Bini, *Electrochim. Acta*, 2019, **296**, 938–944.
- 23 P. Galinetto, D. Spada, M. C. Mozzati, B. Albin and M. Bini, *Opt. Mater. (Amst.)*, 2019, **92**, 373–378.
- 24 R. J. Cava, B. Batlogg, J. J. Krajewski, P. Gammel, H. F. Poulsen, W. F. Peck Jr and L. W. Rupp Jr, *Nature*, 1991, **350**, 598–600.
- 25 R. J. Cava, A. Santoro, D. W. Murphy, S. Zahurak and R. S. Roth, *J. Solid State Chem.*, 1982, **42**, 251–262.
- 26 D. Liu, Z. Shadike, R. Lin, K. Qian, H. Li, K. Li, S. Wang, Q. Yu, M. Liu, S. Ganapathy, X. Qin, Q. Yang, M. Wagemaker, F. Kang, X.-Q. Yang and B. Li, *Adv. Mater.*, 2019, **31**, 1–57.
- 27 J. Purans, A. Kuzmin, E. Cazzanelli and G. Mariotto, *J. Phys. Condens. Matter*, 2007, **19**, 1–8.
- 28 M. G. Stachiotti, F. Cora, C. R. A. Catlow and C. O. Rodriguez, *Phys. Rev. B*, 1997, **55**, 7508–7514.
- 29 S. Rahman, 2015.
- 30 S. Balaji, Y. Djaoued, R. Z. Ferguson and R. Bru, *Chem. Mater.*, 2009, **21**, 1381–1389.
- 31 F. D. Hardcastle and I. E. Wachs, *Solid State Ionics*, 1991, **45**, 201–213.
- 32 M. Kunz and D. Brown, *J. Solid State Chem.*, 1995, **115**, 395–406.
- 33 R. D. Shannon, *Acta Crystallogr.*, 1976, **32A**, 751–767.
- 34 J. E. L. Waldron, M. A. Green and D. A. Neumann, *J. Phys. Chem. Solids*, 2004, **65**, 79–86.
- 35 R. J. Cava, D. W. Murphy and S. M. Zahurak, *J. Electrochem. Soc.*, 1983, **130**, 2345–2351.
- 36 M. Catti, I. Pinus and K. Knight, *J. Solid State Chem.*, 2015, **229**, 19–25.
- 37 M. Catti and M. R. Ghaani, *Phys. Chem. Chem. Phys.*, 2014, **16**, 1385–1392.
- 38 V. Augustyn, P. Simon and B. Dunn, *Energy Environ. Sci.*, 2014, **7**, 1597–1614.
- 39 C. Liu, Z. G. Neale and G. Cao, *Mater. Today*, 2016, **19**, 109–123.
- 40 X. Lou, Q. Fu, J. Xu, X. Liu, C. Lin, J. Han, Y. Luo, Y. Chen, X. Fan and J. Li, *ACS Appl. Nano Mater.*, 2017, acsanm.7b00091.
- 41 X. Lou, R. Li, X. Zhu, L. Luo, Y. Chen, C. Lin, H. Li, X. S. Zhao, R. Li, X. Zhu, L. Luo, Y. Chen, C. Lin, H. Li and X. S. Zhao, *ACS Appl. Mater. Interfaces*, 2019, **11**, 6089–6096.
- 42 S. I. Pyun, H. C. Shin, J. W. Lee and J. Y. Go, in *Electrochemistry of Insertion Materials for Hydrogen and Lithium*, 2012, pp. 11–32.
- 43 M. Nakayama, H. Ikuta, Y. Uchimoto and M. Wakihara, *J. Phys. Chem. B*, 2003, **107**, 10603–10607.

- 44 Metrohm Autolab B. V., *Galvanostatic Intermittent Titration Technique*, 2014.
- 45 X. H. Rui, N. Ding, J. Liu, C. Li and C. H. Chen, *Electrochim. Acta*, 2010, **55**, 2384–2390.
- 46 C. Kim, K. Lee, I. Kim, J. Park, G. Cho, K. Kim, J. Ahn and H. Ahn, *J. Power Sources*, 2016, **317**, 153–158.
- 47 A. P. Hammersley, *ESRF Intern. Rep.*
- 48 A. P. Hammersley, S. O. Svensson, M. Hanfland, A. N. Fitch and D. Häusermann, *High Press. Res.*, 1996, **14**, 235–248.
- 49 A. A. Coelho, 2009.